Title

Molecular Diversity of Sea Spray Aerosol Particles: Impact of Ocean Biology on Particle Composition and Hygroscopicity

Journal

Chem, 2(5)

ISSN

1925-6981

Authors

Cochran, Richard E
Laskina, Olga
Trueblood, Jonathan V
et al.

Publication Date

2017-05-01

DOI

10.1016/j.chempr.2017.03.007

Peer reviewed

Chem

CellPress

Article

Molecular Diversity of Sea Spray Aerosol Particles: Impact of Ocean Biology on Particle Composition and Hygroscopicity

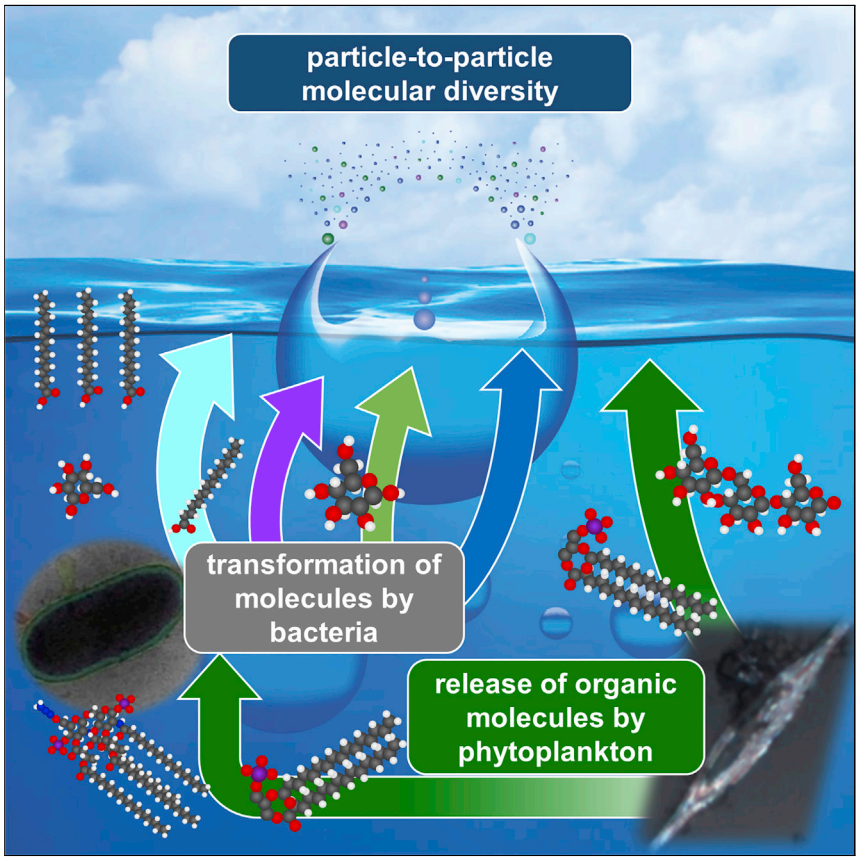

Sea spray aerosol (SSA) particles were found to be diverse with respect to their molecular composition. The number distribution of the SSA particle ensemble, as defined by the molecular signatures in individual particles, shifted in response to changes in the activity of phytoplankton and bacteria in the seawater. This dynamic shift in the molecular composition of individual SSA particles changes their hygroscopicity, a key climate-relevant property.

Richard E. Cochran, Olga Laskina, Jonathan V. Trueblood, ..., Elizabeth A. Stone, Kimberly A. Prather, Vicki H. Grassian

vhgrassian@ucsd.edu

HIGHLIGHTS

The molecular composition of individual nascent SSA particles is diverse

Molecular diversity of individual SSA particles is controlled by the microbial loop

Changes in hygroscopicity of SSA are driven by shifts in particle composition

Cochran et al., Chem 2, 655–667
May 11, 2017
http://dx.doi.org/10.1016/j.chempr.2017.03.007

Chem

CellPress

Article

Molecular Diversity of Sea Spray Aerosol Particles: Impact of Ocean Biology on Particle Composition and Hygroscopicity

Richard E. Cochran,[1] Olga Laskina,[2] Jonathan V. Trueblood,[1] Armando D. Estillore,[1] Holly S. Morris,[2] Thilina Jayarathne,[2] Camille M. Sultana,[1] Christopher Lee,[1] Peng Lin,[3] Julia Laskin,[3] Alexander Laskin,[3] Jacqueline A. Dowling,[2] Zhen Qin,[2] Christopher D. Cappa,[4] Timothy H. Bertram,[5] Alexei V. Tivanski,[2] Elizabeth A. Stone,[2] Kimberly A. Prather,[1] and Vicki H. Grassian[1,6,*]

SUMMARY

The impact of sea spray aerosol (SSA) on climate depends on the size and chemical composition of individual particles that make up the total SSA ensemble. There remains a lack of understanding as to the composition of individual particles within the SSA ensemble and how it changes in response to dynamic ocean biology. Here, we characterize the classes of organic compounds as well as specific molecules within individual SSA particles. The diversity of molecules within the organic fraction was observed to vary between submicrometer- and supermicrometer-sized particles and included contributions from fatty acids, monosaccharides, polysaccharides, and siliceous material. Significant changes in this molecular diversity were observed to coincide with the rise and fall of phytoplankton and heterotrophic bacteria populations within the seawater. Furthermore, the water uptake of individual particles was affected, as learned from studying the hygroscopicity of model systems composed of representative mixtures of salts and organic compounds.

The Bigger Picture

Sea spray aerosol (SSA) particles are an important component of Earth's atmosphere in that they serve as a critical link between the ocean and climate. The key to understanding how SSA affects climate is to unravel the chemical composition and the molecular diversity among individual SSA particles and determine how this influences their climate properties, including particle hygroscopicity. Here, we measured the molecular composition and hygroscopicity of individual SSA particles that were produced in a unique wave-flume facility during periods of dynamic biological activity in seawater. With respect to molecular composition, the number distribution of SSA particle types was seen to be influenced by these biological processes within the seawater. Shifts in the distribution of different particles types led to changes in the average particle hygroscopicity; these changes were further explored via evaluation of the hygroscopicity of model systems containing mixtures of organic compounds and salts.

INTRODUCTION

Anthropogenic aerosols currently constitute only a small fraction of the total aerosol mass across the globe, and natural aerosols are the most prevalent.[1,2] However, anthropogenic aerosols are a substantial fraction of the global aerosol number concentration and can also affect the flux and composition of primary SSA.[3] Determining the extent to which anthropogenic aerosols perturb the global aerosol concentrations requires a better understanding of the contributions from natural aerosol sources. Of the natural sources, sea spray aerosol (SSA) and mineral dust are the major contributors of the total global aerosol mass.[4–8] Primary SSA is formed at the air-sea interface upon the rupturing of bubbles entrained from breaking waves.[9–11] The ability to better define the radiative effects of primary SSA particles will require that their chemical and physical characteristics, as well as their ability to act as cloud condensation nuclei, be established in more detail. With this goal in mind, efforts have focused on characterizing the chemical composition of bulk aerosol across a wide range of marine environments.[4–6,12–18] Global climate models that include primary SSA apply the assumption that aerosols from a single source exhibit the same chemical and physical characteristics.[6,19–21] Recent efforts have challenged this paradigm by showing that individual particles within

the SSA ensemble differ with respect to the relative amount of organic and inorganic constituents as well as phase behavior and morphology.[9,11,22] However, better prediction of aerosol radiative properties and cloud-forming potential will require a better understanding of the particle-to-particle variability in both their exact molecular characteristics and their hygroscopicity.

Primary SSA consists of a mixture of inorganic salts, particulate biological components (e.g., whole bacteria and viruses), and organic matter (OM).[4–6,9,14,22] The OM fraction of SSA depends on size and varies in composition; field studies have reported that the majority of OM in the bulk submicrometer marine aerosol is relatively water insoluble and that in supermicrometer SSA is mostly water soluble.[12–14,23–26] Spectroscopic measurements of SSA particles collected in the field have shown that the oxygen-rich organic fraction of individual particles contains molecules with spectral signatures that are characteristic of saccharides,[24] and signatures for carboxylic acids[26] and alkanes[27] have also been observed.

Oceanic phytoplankton blooms, as identified by chlorophyll a concentrations in seawater, have been linked to increases in the organic fraction of SSA.[16,21,22,28,29] However, in some cases, weak correlations between levels of chlorophyll a and organic content in SSA have been observed.[13,21,27] Recent studies have shown that bacteria-driven alterations of seawater composition lead to changes in both the external and internal mixing state of SSA, as well as particle hygroscopicity.[9,11,14,30–32]

In an effort to provide more detail on the complex molecular composition of individual SSA, we utilized micro-Raman spectroscopy in this study to measure the vibrational spectra of individual freshly emitted SSA particles that had been generated via wave breaking under ocean-relevant bloom conditions in an enclosed wave flume. By integrating single-particle Raman spectroscopy with the analysis of bulk particle samples via a range of quantitative methods, we went beyond functional-group analysis to gain insights into the major classes of organic molecules and their molecular structures that constitute nascent SSA. With this, we report on the diversity of organic molecules in size-dependent SSA from both single-particle and bulk-aerosol perspectives. Furthermore, we show the changing composition of freshly emitted SSA across a broad range of biological conditions. On the basis of this analysis, we define how specific auto- and heterotrophic processes that occur within the ocean directly influence the composition of the SSA. Our article is divided into two sections: (1) defining the molecular diversity of individual SSA particles and connecting temporal variations in the number distribution of SSA particles to dynamic ocean compositions and (2) linking the observed temporal trends in the molecular composition of individual SSA particles to their hygroscopic properties.

RESULTS AND DISCUSSION

Molecular Diversity within the SSA Ensemble and Connections to Dynamic Ocean Biology

Using state-of-the-art methods, we probed the molecular composition of individual freshly emitted SSA particles collected from a wave-flume facility at different periods throughout a phytoplankton bloom. This section first describes the observed molecular diversity of individual particles and then compares the observed changes in this diversity with changes in the measured concentrations of auto- and heterotrophic species in seawater. To help support the connection between ocean biology dynamics and the molecular diversity in SSA particles, we discuss the biological sources

[1]Department of Chemistry and Biochemistry, University of California, San Diego, La Jolla, CA 92093, USA

[2]Department of Chemistry, University of Iowa, Iowa City, IA 52242, USA

[3]William R. Wiley Environmental Molecular Sciences Laboratoryand Physical Sciences Division, Pacific Northwest National Laboratory, Richland, WA 99354, USA

[4]Department of Civil and Environmental Engineering, University of California, Davis, Davis, CA 95616, USA

[5]Department of Chemistry, University of Wisconsin–Madison, Madison, WI 53706, USA

[6]Lead Contact

*Correspondence: vhgrassian@ucsd.edu

http://dx.doi.org/10.1016/j.chempr.2017.03.007

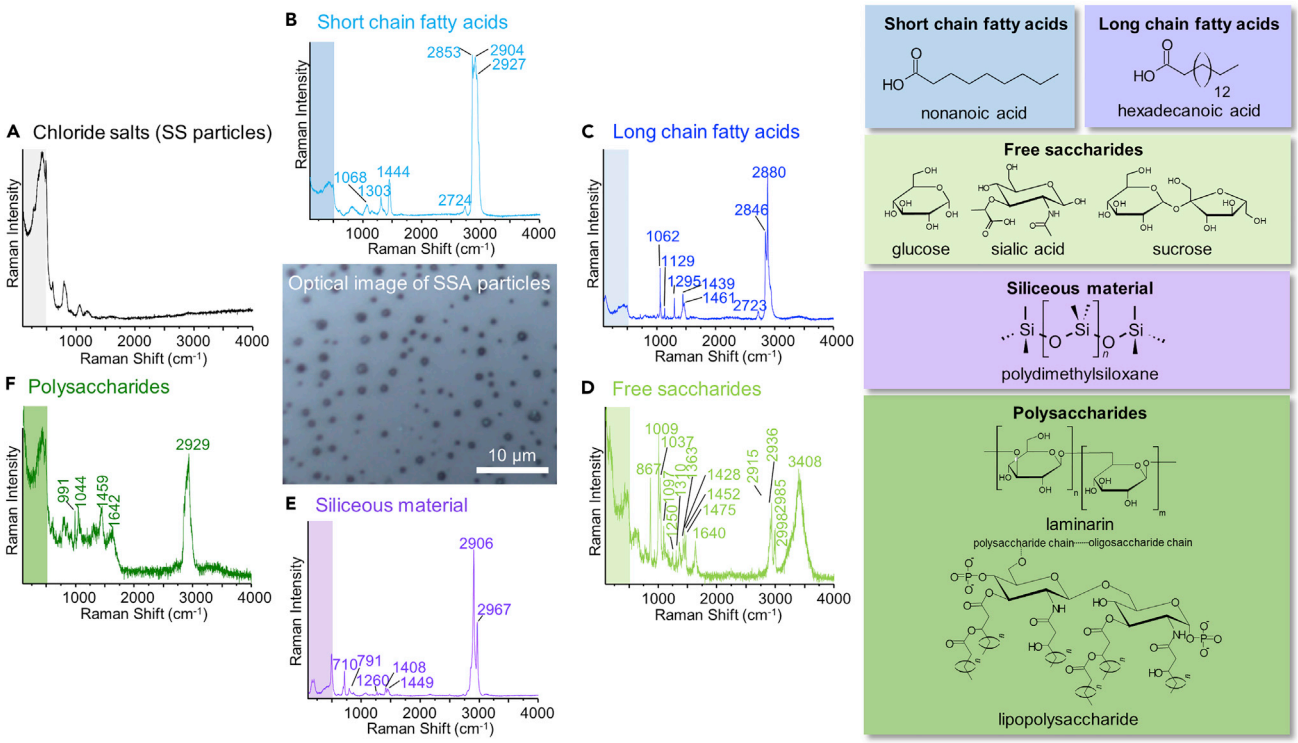

Figure 1. Representative Raman Spectra of Individual SSA Particles

Six types of Raman signatures observed for 560–1,000 nm and 1.8–3.2 μm SSA particles collected on a quartz substrate during a month-long mesocosm experiment: (A) chloride salts (SS particles), (B) short-chain fatty acids, (C) long-chain fatty acids, (D) free saccharides, (E) siliceous material, and (F) polysaccharides. Organic components identified include short-chain fatty acids, long-chain fatty acids, free saccharides, siliceous material, and polysaccharides. Each spectrum shown was recorded from a single particle within the SSA ensemble for an average of two separate exposures at 5–10 s each and recorded in the range of 100–4,000 cm^{-1}. The region below 500 cm^{-1} (shaded) contains significant contributions from background spectral features that are attributed to either NaCl or the quartz substrates and were not considered when the identity of the class of organic molecules was determined. See also Figures S1–S5 and Tables S1 and S2.

of observed molecules in SSA. Finally, we propose a pathway connecting biological processes to particle composition.

With respect to the presence of Raman spectral features specific to organic compounds (Figure 1; see Table S2 for additional information), all of the SSA particles collected from the wave flume can be divided into two broad categories. The first category of particles did not exhibit any Raman spectral signatures associated with organic molecules and was thus composed of nearly pure sea salt (SS). Of note, all spectral signals below 500 cm^{-1} were attributed to the quartz substrate. The second category exhibited distinguishable Raman signatures associated with C-H vibrations, indicating a mixture of organic material with SS (referred to as SS-OC particles). Most of the SSA particles that were analyzed included spectral signatures from the co-presence of organic compounds (i.e., SS-OC particles, of which only 0%–1.5% and 0%–7.5% of submicrometer and supermicrometer SSA particles, respectively, were SS particles).

Representative Raman spectra for SS-OC particles are summarized in Figure 1 (see Raman spectral assignments in the Supplemental Experimental Procedures and Table S2). For SS-OC particles, five main particle types were identified on the basis of the comparison of Raman signatures of individual SSA particles with those obtained from the analysis of more than 25 representative model systems (described

in detail in the Supplemental Experimental Procedures; also see the spectra presented in Figures S1–S5). These particle types included (1) long-chain saturated fatty acids ($C_{12–18}$), (2) short-chain saturated fatty acids ($C_{5–10}$), (3) saccharides (including oligosaccharides and polysaccharides), (4) mono- and disaccharides (which we refer to here as "free saccharides"; they contain hydroxyl groups that, in the marine environment, are often substituted with amine, amide, carboxylate, sulfate, and other functional groups[33,34]), and (5) siliceous material (biosilica structures such as exoskeletons or frustules). In addition to the SS and SS-OC particle types, a small fraction (1%–27% of submicrometers and 7%–23% of supermicrometers) were either highly fluorescent or pyrolyzed during analysis and thus were unable to be categorized.

On the basis of the chemical speciation identified by Raman spectroscopy, the organic fractions of individual particles were separated into two classes: aliphatic rich (relatively low O/C values; <0.2) or oxygen rich (relatively high O/C values; ≥0.2). Long-chain carboxylic acids ($\geq C_{10}$) are operationally defined in this work as aliphatic-rich species, whereas the rest of the tentatively identified classes of organic molecules (i.e., free saccharides, polysaccharides, siliceous material, and short-chain fatty acids) are relatively more oxygen-rich species. Number fractions of SS-OC particles exhibiting spectral features for aliphatic-rich and oxygen-rich organic compounds were determined (an example for SSA collected in a single day from the wave flume is shown in Figure S6). In submicrometer SSA, spectral signatures for aliphatic-rich species were the most prominent, in that as much as 75% of submicrometer particles exhibited strong signals for long-chain fatty acids either in the protonated or deprotonated form (Figure 2A). In contrast, up to 88% of supermicrometer SSAs were dominated by oxygen-rich species (Figure 2B). Some particles showed mixtures of aliphatic-rich and oxygen-rich species, in that 4%–17% and 3%–46% of sub- and supermicrometer particles, respectively, exhibited strong spectral signatures for both free saccharides and short-chain fatty acids (Figure 2).

To support the accurate identification of organic species by Raman spectroscopy, measurements of organic compounds were made for bulk SSA of the same (or similar) size ranges collected from the wave flume during the first phytoplankton bloom. With a variety of techniques, C_4–C_{24} fatty acids (Figure S7), saccharides (comprising mono-, oligo-, and polysaccharides),[35] C_{14}–C_{40} alkanes, and individual inorganic salts (Na^+, K^+, Mg^{2+}, Ca^{2+}, Cl^-, and SO_4^{2-})[35] were observed and quantified in bulk SSA.

Characterizing the molecular composition of particles within SSA collected during a controlled mesocosm devoid of anthropogenic and terrestrial influences provides a unique opportunity to assess the effect of biological processes on SSA chemistry. The molecular diversity of individual particles collected during the wave-flume experiment, which included two consecutive oceanic phytoplankton blooms, was observed to change in response to fluctuations in the concentration of phytoplankton (autotrophs) and heterotrophic bacteria. Figure 2 shows the changes in the distribution of major organic classes observed with Raman analysis of SSA collected from the wave flume overlaid on the measured concentrations of chlorophyll a (a tracer for phytoplankton activity[29]) and heterotrophic bacteria in the seawater, as well as online measurements of the size-resolved bulk chemical composition by aerosol mass spectrometry (AMS).[31] The number of individual SSA particles that were analyzed each day is provided in Table S1. During the beginning of the first bloom, only 32% of the submicrometer particles contained long-chain fatty acid Raman signatures. Smaller fractions of other particle types included polysaccharides (14%), siliceous material (13%), and a mixture of free saccharides and short-chain

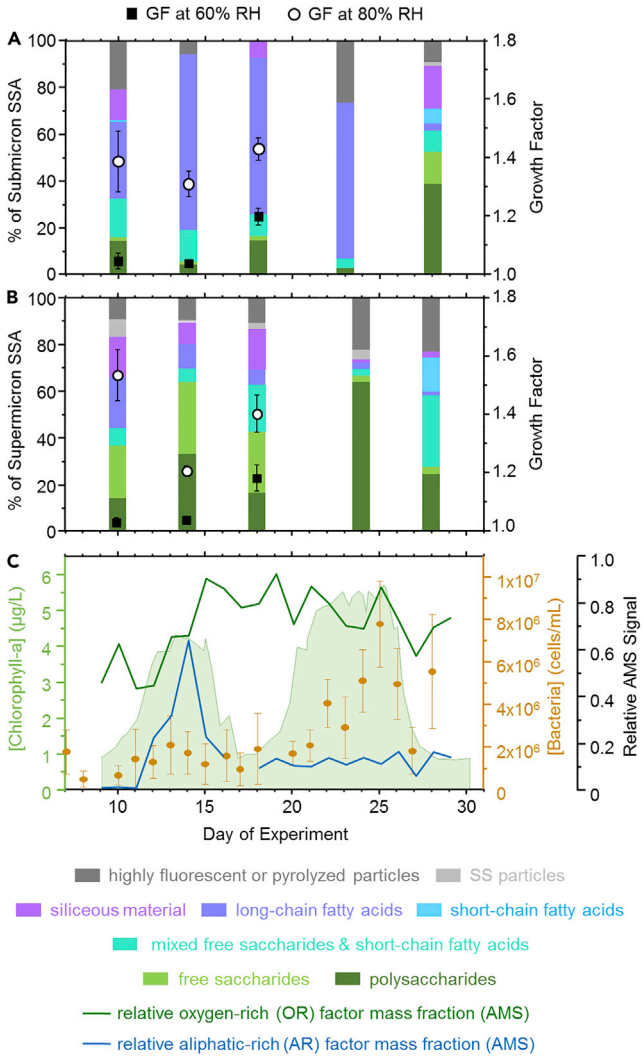

Figure 2. Shifts in the Molecular Speciation within Individual SSA Particles in Response to Changes in the Concentration of Phytoplankton and Heterotrophic Bacteria

(A and B) Changes in the composition of individual (A) submicrometer (0.56–1.00 μm) and (B) supermicrometer (1.8–3.2 μm) particles within SSA collected on different days throughout the mesocosm. Each class of organic and inorganic compound is shown as a percentage of particles within the SSA ensemble that exhibit Raman signatures for that particular class. The remaining fraction of particles was highly fluorescent or pyrolyzed during Raman analysis. The average hygroscopic growth factors of individual submicrometer (0.5–1.0 μm) and supermicrometer (>1.0 μm) SSA particles collected from the wave flume as determined by offline AFM analysis are also shown in both (A) and (B). Error bars represent one standard deviation calculated from all growth factor measurements for particles within that size range.

(C) The measurements of chlorophyll a and heterotrophic bacteria concentrations in the seawater of the wave flume, along with aliphatic-rich and oxygen-rich factor mass fractions as determined through the online measurement of the size-resolved bulk chemical composition of SSA by AMS. The AMS factor mass fractions are reproduced with permission from Wang et al.[31] See also Figures S1–S6 and Tables S1–S3.

fatty acids (17%). The fraction of long-chain fatty acid particles increased significantly during the first bloom (up to 75%). Interestingly, the relative fraction of these aliphatic-rich particles remained similar between the two blooms (67%) and through the second bloom (67%). This is in contrast to the relatively rapid decrease in the relative mass fraction of aliphatic-rich species (as defined by mass spectra

dominated by hydrocarbon peaks from AMS) from 0.64 to 0.22 over a 1-day period at the end of the first bloom (Figure 2C). The disparity between the measurements of individual particles and bulk SSA provides evidence that changes in the normalized organic mass fraction of bulk SSA are not necessarily reflected in the external mixing state of individual particles in the SSA. Alternatively, this also suggests that the SSA particle-size range responsible for the dramatic decrease in aliphatic-rich components in bulk submicrometer SSA (particles with aerodynamic diameters between 0.06 and 1.5 μm at a relative humidity [RH] of 80%) could differ from that evaluated here with Raman spectroscopy (between 0.56 and 1.0 μm at 80% RH). After the second bloom, a sharp decrease was observed in the fraction of the SSA population containing particles with signatures of long-chain fatty acids. During the same time period, the aliphatic-rich signal of the bulk submicrometer SSA analyzed with AMS did not significantly change (between 0.14 and 0.16; Figure 2C).

Unlike the submicrometer SSA, supermicrometer SSA displayed substantial differences between the two blooms. During the first bloom, the distribution between the classes of oxygen-rich species changed only slightly, and only a small fraction contained aliphatic-rich compounds. During the second bloom, supermicrometer SSA particles were dominated by polysaccharides but contained smaller fractions of other oxygen-rich particle types. The increase in polysaccharides and decrease in siliceous material in the supermicrometer SSA coincide with the rise in heterotrophic bacteria levels observed in the wave flume during the second bloom.

The observed variation in the molecular distribution of individual particles described above can be connected to the dynamic microbial processes in the seawater via consideration of their auto- and heterotrophic sources. To better assess the contribution of these sources, we complemented single-particle analysis with offline techniques characterizing the bulk SSA. Using high-resolution mass spectrometry in conjunction with gas chromatography-mass spectrometry allowed identification and quantification of a homologous series of fatty acids ranging from octanoic acid (C_8) to tetracosanoic acid (C_{24}) in the bulk SSA.[36] The absolute distribution of saturated fatty acids (Figure S7) followed those previously observed in the organic fractions of seawater and marine aerosols collected in the field.[18,37] In the ocean, free fatty acids (i.e., alkanoic acids) have been observed to be a major fraction of the organic compounds present[38–42] and are produced by the heterotrophic breakdown of lipid-containing cellular components of microorganisms, such as phospholipids, glycolipids, and triacylglycerides. Although the aliphatic-rich component of SSA analyzed via online AMS was hypothesized to include triacylglycerides,[31] Raman spectra obtained in this study for individual SSA particles did not exhibit their specific signatures. Note, however, that triacylglycerides can be easily oxidized and/or hydrolyzed before offline analysis, and thus it cannot be concluded that triacylglycerides were not originally transferred to the SSA. Relative to the other classes of molecules identified in this work, long-chain fatty acids exhibited significantly increased surface activity, resulting in their enrichment in the sea-surface microlayer. This provides efficient transfer of the long-chain fatty acids into film drops (typically <1 μm in diameter) during the bubble-bursting process at the air-sea interface. This physicochemical behavior explains the consistently large fraction of submicrometer SSA particles that exhibited Raman signatures for long-chain fatty acids.

Small-chain fatty acids with even carbon numbers (e.g., C_8 and C_{10}) have also been observed to occur from biological sources.[40] Nonanoic acid, for the most part, has not been previously observed from sources within ocean biota and is suggested to be produced mainly from the oxidation of C_{18} unsaturated fatty acids (Equation 1).[43]

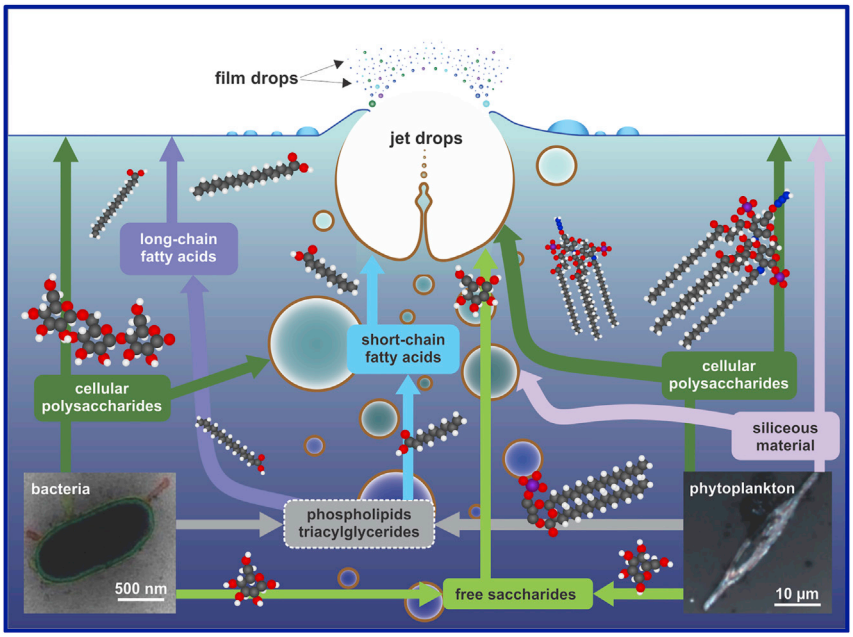

Figure 3. Linking Microbial Chemical Pathways to the Molecular Diversity of Individual SSA Particles

Degradation pathways of diatoms and bacteria lead to organic species that are transported from seawater to SSA particles as either film or jet drops. Boxes with a dashed outline were not directly observed in this work but are shown here as a precursor to classes of compounds that were observed.

$$CH_3(CH_2)_7CH=CH(CH_2)_7COOH \xrightarrow{h\nu, O_2} C_8H_{17}COOH + OHCC_7H_{14}COOH \quad \text{(Equation 1)}$$

The siliceous material observed in SSA particles is suggested here to be a product of diatoms (known to be one of the largest groups of silicifying organisms) taking up silica in vast quantities and subsequently bioprocessing it into useful biosilica structures such as exoskeletons or frustules.[44] Upon cell death, the frustules release siliceous material into the water column, which can either be transferred into SSA or further transformed through heterotrophic processes.

Saccharides observed in this study, and previously observed in the sea-surface microlayer and marine aerosols, have been suggested to be in the polymeric or oligomeric form[24,26,45–48] and can exist as cellular polysaccharides (e.g., laminarin, chrysolaminarin, chitin, lipopolysaccharides, alginic acid, and dextrose) or extracellular polymeric substances (EPSs).[14,33,46,49,50] Whereas cellular polysaccharides have a more defined structure, the structure of EPSs is recognized as being either a polysaccharide or a glycoconjugate (viscous or gelatinous mixture of saccharides) and is therefore difficult to identify explicitly.[50,51] Within the mesocosm, saccharides (including mono-, oligo-, and polysaccharides) accounted for 8% of the total organic carbon of the bulk SSA below 2.5 μm, and the remaining 92% has yet to be determined. Of note,lipopolysaccharide (LPS) which contains a polysaccharide and oligosaccharide core[52–55] also contains fatty acid ester side chains.[53,55,56]

In considering the variations in both the time- and size-resolved compositions, as well as the various biological sources discussed above, we propose a comprehensive and dynamic pathway between ocean biology and SSA particle composition (Figure 3). Upon the death of phytoplankton, particulate forms of

lipids, polysaccharides, and siliceous material are released into the bulk seawater. Autotrophic enzyme digestion releases fatty acids from higher-order lipids while generating smaller fragments of cellular poly- and oligosaccharides. Heterotrophic bacteria then further contribute free fatty acids and smaller saccharide fragments through the efficient enzymatic digestion of phytoplankton, and to some extent bacterial, components.[53,54,56–58] The heterotrophic degradation of polysaccharides into smaller oligosaccharide fragments helps explain the dramatic increase in the fraction of polysaccharide-type particles in submicrometer SSA collected before and after the peak in the bacteria concentration.

Many of the pathways described above as biological sources of the molecules observed in SSA particles are centered around the major role of heterotrophic degradation processes within bacterial cells. Given that the turnover rate for these enzyme processes is typically high, it is assumed that the limiting factor in the heterotrophic chemical transformation of the ocean water is the relative concentration of heterotrophic bacteria. The observed response of the molecular diversity of SSA particles to changes in ocean biology shows a clearer link between auto- and heterotrophic activity and single-particle composition. These dynamic changes in particle compositions can, in turn, affect their physicochemical properties, including their interaction with water vapor, a key climate-relevant property.

Interparticle Variability of SSA and Influence on Hygroscopic Growth

Using a novel method to characterize the single-particle hygroscopicity, we compared the average hygroscopicity of the particle ensemble with temporal changes in the number fraction of particle types (shown in Figure 2 for both sub- and supermicrometer SSA particles). The hygroscopic growth factors of individual particles as determined by atomic force microscopy (AFM; see additional method details in Morris et al.[59]) at RH = 80% (growth factors = 80%) of both sub- and supermicrometer particles collected from the wave flume decreased from 1.39 $\pm$ 0.11 and 1.53 $\pm$ 0.09, respectively, before the first phytoplankton bloom to 1.31 $\pm$ 0.04 and 1.20 $\pm$ 0.02, respectively, during the bloom. After the first bloom, the growth factors then increased to 1.43 $\pm$ 0.04 and 1.40 $\pm$ 0.06 for sub- and supermicrometer particles, respectively. The changes in the measured hygroscopicity of individual particles of the same size range during the progression of the first phytoplankton bloom can be explained by the relative changes in the number fraction of particles types with respect to the observed classes of organic molecules. Recent work has shown that the ability of an SSA particle to take up water is directly correlated with the hygroscopicity (represented by kappa [κ] values) of the organic and inorganic fractions, where the overall particle hygroscopicity is a linear combination of the κ values for each compound present.[60,61] In this study, κ values calculated from laboratory measurements of particle hygroscopic growth factors of SSA mimics with a hygroscopic tandem differential mobility analyzer (HTDMA) show that surface-active species observed in SSA particles from the wave flume, such as long-chain fatty acids and polysaccharides, exhibit decreased hygroscopicity in relation to free saccharides (Table 1). These calculated κ values help explain the observed changes in the average and range of hygroscopicities of individual SSA particles collected during the wave-flume experiment. For example, the increase in the fraction of submicrometer particles dominated by the relatively more surface-active and less hygroscopic long-chain fatty acid particles from day 10 to day 14 resulted in a lower average hygroscopicity and a narrower growth factor distribution. Furthermore, the increase in the average water uptake of individual submicrometer SSA particles from day 14 to

Table 1. Hygroscopic Growth Factors at 60% and 80% RH at T = 298 K of Particles Representative of the Individual SSA Particle Types Collected during the Wave-Flume Experiment

Representative Compound or Mixture[a]	Particle Type[b]	Hygroscopicity Parameter (κ; 80% RH)	Measured Growth Factor[c]	
			60% RH	80% RH
NaCl	SS	1.32	1.00 ± 0.06	2.00 ± 0.04
Reef salt	SS	1.28	1.12 ± 0.08	1.80 ± 0.05
NaCl/nonanoic acid (2:1)	SS-OC	1.27	1.01 ± 0.10	1.91 ± 0.12
NaCl/nonanoic acid (1:1)	SS-OC	1.13	0.99 ± 0.10	1.74 ± 0.11
NaCl/glucose (2:1)	SS-OC	0.86	1.04 ± 0.10	1.62 ± 0.03
NaCl/alginate (2:1)	SS-OC	0.71	1.01 ± 0.08	1.54 ± 0.03
NaCl/LPS (1:1)	SS-OC	0.50	1.01 ± 0.10	1.42 ± 0.03
Glucose	OC	0.20	1.20 ± 0.02	1.20 ± 0.02
Sodium alginate	OC	0.13	1.14 ± 0.04	1.14 ± 0.04
LPS	OC	0.081	1.09 ± 0.05	1.09 ± 0.05
Laminarin	OC	0.026	1.00 ± 0.08	1.03 ± 0.06
Hexadecanoic acid	OC	–	~1	~1

LPS, liposaccharide; RH, relative humidity.

[a]Ratios in parentheses refers to the mass ratios of the constituents.

[b]Particle types refer to SSA containing only sea salt (SS), only organic carbon (OC), or a mixture of organic carbon and SS (SS-OC).

[c]Growth factor values were determined through measurements by HTDMA and were used for calculating the hygroscopicity parameters for each compound or mixture.

day 18 can be a result of the observed decrease in the long-chain fatty acid fraction and increase in the more hygroscopic polysaccharide fraction. For supermicrometer particles, the decrease in the polysaccharide fraction and increase in the short-chain fatty acid and free saccharide fractions with larger κ values (according to the values for the NaCl/organic mixtures shown in Table 1) led to an increase in the average water uptake of the SSA particles. Alternatively, the hygroscopicity could be influenced by changes in the molar ratios between inorganic salts and organic components. This effect is demonstrated in Figure 4 for representative model aerosol systems composed of NaCl and either glucose or laminarin at different mass ratios. For both systems, the increase in the relative fraction of the organic constituent decreased the particle hygroscopicity. The above observation highlights the phenomena that the average and distribution of the measured hygroscopicity of individual particles change in response to observed changes in the molecular diversity of particle types.

Linking Ocean Biology, SSA Chemistry, and Climate

Using methods to probe the chemical composition of individual SSA particles and integrating them with other analytical techniques, we have extended the discussion beyond functional-group analysis utilized in previous studies to identify the specific major classes of organic molecules within SSA particles as a function of ocean biology.

The results from this study demonstrate the particle-to-particle variation in the chemical composition of SSA particles as a function of particle size and biological activity within seawater. Furthermore, in coupling techniques for probing the molecular composition and subsaturated hygroscopicity of individual SSA particles, we have shown a more direct link between changing ocean chemistry, particle composition, and hygroscopicity. This detailed understanding of the molecular composition of nascent SSA will guide

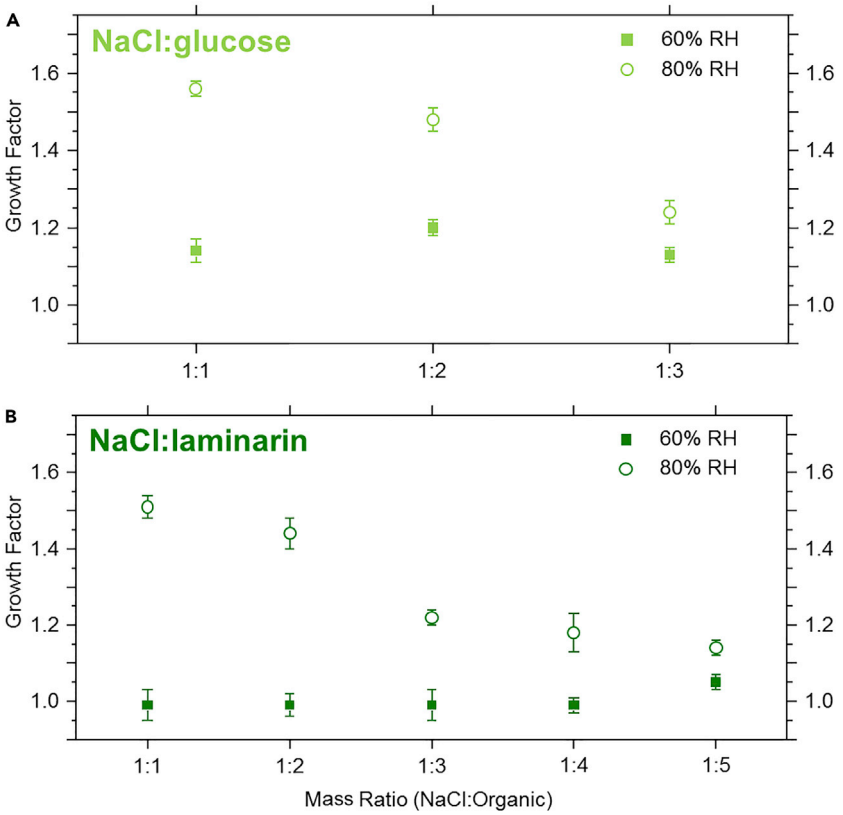

Figure 4. Hygroscopicity of Particles Composed of Representative Mixtures of Salts and Organic Compounds: Fatty Acids and Simple and Complex Saccharides

Hygroscopic growth factors of representative laboratory-generated aerosol containing NaCl and mixed mass ratios (NaCl/organic) of either (A) glucose (representative or free saccharides) or (B) laminarin (representative of polysaccharides). Measured growth factors at both 60% and 80% RH at 298 K are shown. All growth factor measurements were made by HTDMA. Error bars represent standard deviations calculated from the growth factors determined in triplicate experiments.

future work aimed at establishing a framework for the mechanisms by which molecules are transferred from the ocean to SSA. Realizing the diversity in the molecular compositions of individual SSA particles and the interplay between particle composition and hygroscopicity is important in furthering our understanding of the impacts of SSA on climate and the environment. However, to better define the link between ocean biology and climate, future experiments coupling observations of ocean biology and SSA composition to measurements of SSA flux and the secondary chemical transformations of SSA particles are needed.

EXPERIMENTAL PROCEDURES

SSA particles of similar size and composition to those measured in the atmosphere were generated via wave breaking during an oceanic phytoplankton bloom conducted within a unique ocean-relevant wave flume at the Hydraulics Laboratory at the Scripps Institution of Oceanography. SSA was sampled from the wave flume by a series of online instruments measuring their physicochemical properties. This included measurement of the SSA size distribution by a scanning mobility particle sizer and an aerodynamic particle sizer, determination of SSA particle mixing state with an aerosol time-of-flight mass spectrometer, and chemical composition of bulk SSA with an Aerodyne high-resolution time-of-flight aerosol mass

spectrometer. Bulk seawater measurements were made throughout the wave-flume experiment for quantifying the abundance of phytoplankton (via fluorometric measurement of chlorophyll a concentration) and enumerating bacteria by epi-fluorescence microscopy. In-depth details of the wave-flume experiment, as well as the online instrumentation and bulk seawater measurements, can be found in Wang et al.[31] In addition to the online measurements, SSA particles were also collected for offline measurements of their physicochemical properties and chemical composition. Offline single-particle probing of the functional-group composition of the organic fraction of SSA was performed by Raman spectroscopy. The hygroscopicity of single SSA particles was measured by AFM, as recently described in Morris et al.[59] The phase morphology of individual SSA particles was also determined by AFM. The total organic carbon concentration in bulk SSA was measured with a Sunset Laboratory thermal optical analyzer. Identification of fatty acids in bulk SSA was made possible with an electrospray linear ion-trap orbitrap mass spectrometer (ESI-LIT-Orbitrap). Concentration measurements of individual saturated and unsaturated fatty acids and saturated alkanes in bulk SSA were made by gas-chromatography mass spectrometry. Total saccharide concentrations in bulk SSA were made by ion-exchange chromatography (IEC) with electrochemical detection. Concentrations of individual inorganic salts were also measured by IEC with conductivity detection. The total SS concentration was the sum of the major individual inorganic salts (Na^+ + K^+ + Mg^{2+} + Ca^{2+} + Cl^- + $SO4^{2-}$) collected from the wave flume. Mimic SSAs were generated from aqueous solutions with an atomizer, and their hygroscopicities were measured with an HTDMA. Further details for the offline methods listed here can be found in the Supplemental Experimental Procedures.

SUPPLEMENTAL INFORMATION

Supplemental Information includes Supplemental Experimental Procedures, seven figures, and three tables and can be found with this article online at http://dx.doi.org/10.1016/j.chempr.2017.03.007.

AUTHOR CONTRIBUTIONS

R.E.C. and O.L. are co-first authors. Project Administration, V.H.G., K.A.P., T.H.B, E.A.S., A.T., and C.D.C.; Resources, J.L. and A.L.; Investigation, R.E.C., O.L., J.T., A.E., T.J., H.M., C.M.S., C.L., J.D., Z.Q., and P.L.; Formal Analysis, R.E.C., O.L., J.T., A.E., H.M., and T.J.; Writing – Original Draft, R.E.C., O.L., and V.H.G.; Writing – Review & Editing, R.E.C. and V.H.G.

ACKNOWLEDGMENTS

We thank Professor Ryan Moffet for helpful discussion in interpreting our findings. We also would like to acknowledge Dr. Joseph Patterson for providing the image for bacteria shown in Figure 3. This work was funded by the National Science Foundation through the Center for Aerosol Impacts on Climate and the Environment under grant no. CHE 1305427. The high-resolution mass spectrometry experiments described in this paper were partially performed in the Environmental Molecular Sciences Laboratory, a national scientific user facility sponsored by the Office of Biological and Environmental Research of the US Department of Energy (DOE) and located at the Pacific Northwest National Laboratory (PNNL). PNNL is operated for the US DOE by Battelle Memorial Institute under contract no. DE-AC06-76RL0 1830. Any opinions, findings, and conclusions or recommendations expressed in this material are those of the authors and do not necessarily reflect the views of the National Science Foundation.

Received: November 18, 2016
Revised: January 12, 2017
Accepted: March 10, 2017
Published: May 11, 2017

REFERENCES AND NOTES

1. Pandis, S.N., and Seinfeld, J.H. (2006). Atmospheric Chemistry and Physics, Second Edition (John Wiley).

2. Finlayson-Pitts, B.J., and Pitts, J.N., Jr. (2000). Upper and Lower Atmosphere, First Edition (Academic Press).

3. Mårtensson, E.M., Nilsson, E.D., de Leeuw, G., Cohen, L.H., and Hansson, H.-C. (2003). Laboratory simulations and parameterization of the primary marine aerosol production. J. Geophys. Res. *108*, 1–12.

4. Quinn, P.K., Collins, D.B., Grassian, V.H., Prather, K.A., and Bates, T.S. (2015). Chemistry and related properties of freshly emitted sea spray aerosol. Chem. Rev. *115*, 4383–4399.

5. Gantt, B., and Meskhidze, N. (2013). The physical and chemical characteristics of marine primary organic aerosol: a review. Atmos. Chem. Phys. *13*, 3979–3996.

6. de Leeuw, G., Andreas, E.L., Anguelova, M.D., Fairall, C.W., Lewis, E.R., Dowd, C.O., Schulz, M., and Schwartz, S.E. (2011). Production flux of sea spray aerosol. Rev. Geophys. *49*, http://dx.doi.org/10.1029/2010RG000349, RG2001.

7. Intergovernmental Panel on Climate Change. IPCC Fifth Assessment Report; 2013. https://www.ipcc.ch/report/ar5/.

8. Cwiertny, D.M., Young, M.A., and Grassian, V.H. (2008). Chemistry and photochemistry of mineral dust aerosol. Annu. Rev. Phys. Chem. *59*, 27–51.

9. Collins, D.B., Zhao, D.F., Ruppel, M.J., Laskina, O., Grandquist, J.R., Modini, R.L., Stokes, M.D., Russell, L.M., Bertram, T.H., Grassian, V.H., et al. (2014). Direct aerosol chemical composition measurements to evaluate the physicochemical differences between controlled sea spray aerosol generation schemes. Atmos. Meas. Tech. *7*, 3667–3683.

10. Callaghan, A.H., Stokes, M.D., and Deane, G.B. (2014). The effect of water temperature on air entrainment, bubble plumes, and surface foam in a laboratory breaking-wave analog. J. Geophys. Res. Atmos. *119*, 7463–7482.

11. Prather, K.A., Bertram, T.H., Grassian, V.H., Deane, G.B., Stokes, M.D., Demott, P.J., Aluwihare, L.I., Palenik, B.P., Azam, F., Seinfeld, J.H., et al. (2013). Bringing the ocean into the laboratory to probe the chemical complexity of sea spray aerosol. Proc. Natl. Acad. Sci. USA *110*, 7550–7555.

12. Cavalli, F., Facchini, M.C., Decesari, S., Mircea, M., Emblico, L., Fuzzi, S., Ceburnis, D., Yoon, Y.J., O'Dowd, C.D., Putaud, J.P., et al. (2004). Advances in characterization of size-resolved organic matter in marine aerosol over the North Atlantic. J. Geophys. Res. D Atmos. *109*, 1–14.

13. Vignati, E., Facchini, M.C., Rinaldi, M., Scannell, C., Ceburnis, D., Sciare, J., Kanakidou, M., Myriokefalitakis, S., Dentener, F., and O'Dowd, C.D. (2010). Global scale emission and distribution of sea-spray aerosol: sea-salt and organic enrichment. Atmos. Environ. *44*, 670–677.

14. Facchini, M.C., Rinaldi, M., Decesari, S., Carbone, C., Finessi, E., Mircea, M., Fuzzi, S., Ceburnis, D., Flanagan, R., Nilsson, E.D., et al. (2008). Primary submicron marine aerosol dominated by insoluble organic colloids and aggregates. Geophys. Res. Lett. *35*, L17814.

15. Facchini, M.C., Decesari, S., Rinaldi, M., Carbone, C., Finessi, E., Mircea, M., Fuzzi, S., Moretti, F., Tagliavini, E., Ceburnis, D., et al. (2008). Important source of marine secondary organic aerosol from biogenic amines. Environ. Sci. Technol. *42*, 9116–9121.

16. O'Dowd, C.D., Jimenez, J.L., Bahreini, R., Flagan, R.C., Seinfeld, J.H., Hameri, K., Pirjola, L., Kulmala, M., Jennings, S.G., and Hoffmann, T. (2002). Marine aerosol formation from biogenic iodine emissions. Nature *417*, 632–636.

17. Mochida, M., Umemoto, N., Kawamura, K., Lim, H.-J., and Turpin, B.J. (2007). Bimodal size distributions of various organic acids and fatty acids in the marine atmosphere: influence of anthropogenic aerosols, Asian dusts, and sea spray off the coast of East Asia. J. Geophys. Res. *112*, 209.

18. Mochida, M., Kitamori, Y., Kawamura, K., Nojiri, Y., and Suzuki, K. (2002). Fatty acids in the marine atmosphere: factors governing their concentrations and evaluation of organic films on sea-salt particles. J. Geophys. Res. Atmos. *107*, 4325.

19. Lewis, E.R., and Schwartz, S.E. (2004). Sea Salt Aerosol Production: Mechanisms, Methods, Measurements and Models, First Edition (American Geophysical Union).

20. Jaeglé, L., Quinn, P.K., Bates, T.S., Alexander, B., and Lin, J.-T. (2011). Global distribution of sea salt aerosols: new constraints from in-situ and remote sensing observations. Atmos. Chem. Phys. *11*, 3137–3157.

21. O'Dowd, C.D., Langmann, B., Varghese, S., Scannell, C., Ceburnis, D., and Facchini, M.C. (2008). A combined organic-inorganic sea-spray source function. Geophys. Res. Lett. *35*, 1–5.

22. Ault, A.P., Moffet, R.C., Baltrusaitis, J., Collins, D.B., Ruppel, M.J., Cuadra-Rodriguez, L.A., Zhao, D., Guasco, T.L., Ebben, C.J., Geiger, F.M., et al. (2013). Size-dependent changes in sea spray aerosol composition and properties with different seawater conditions. Environ. Sci. Technol. *47*, 5603–5612.

23. Russell, L.M., Bahadur, R., and Ziemann, P.J. (2011). Identifying organic aerosol sources by comparing functional group composition in chamber and atmospheric particles. Proc. Natl. Acad. Sci. USA *108*, 3516–3521.

24. Russell, L.M., Hawkins, L.N., Frossard, A.A., Quinn, P.K., and Bates, T.S. (2010). Carbohydrate-like composition of submicron atmospheric particles and their production from ocean bubble bursting. Proc. Natl. Acad. Sci. USA *107*, 6652–6657.

25. O'Dowd, C.D., Facchini, M.C., Cavalli, F., Ceburnis, D., Mircea, M., Decesari, S., Fuzzi, S., Yoon, Y.J., and Putaud, J.-P. (2004). Biogenically driven organic contribution to marine aerosol. Nature *431*, 676–680.

26. Hawkins, L.N., and Russell, L.M. (2010). Polysaccharides, proteins, and phytoplankton fragments: four chemically distinct types of marine primary organic aerosol classified by single particle spectromicroscopy. Adv. Meteorol. *2010*, 1–14.

27. Quinn, P.K., Bates, T.S., Schulz, K.S., Coffman, D.J., Frossard, A.A., Russell, L.M., Keene, W.C., and Kieber, D.J. (2014). Contribution of sea surface carbon pool to organic matter enrichment in sea spray aerosol. Nat. Geosci. *7*, 228–232.

28. Ovadnevaite, J., Ceburnis, D., Martucci, G., Bialek, J., Monahan, C., Rinaldi, M., Facchini, M.C., Berresheim, H., Worsnop, D.R., and O'Dowd, C.D. (2011). Primary marine organic aerosol: a dichotomy of low hygroscopicity and high CCN activity. Geophys. Res. Lett. *38*, 1–5.

29. Rinaldi, M., Fuzzi, S., Decesari, S., Marullo, S., Santoleri, R., Provenzale, A., Von Hardenberg, J., Ceburnis, D., Vaishya, A., O'Dowd, C.D., et al. (2013). Is chlorophyll-a the best surrogate for organic matter enrichment in submicron primary marine aerosol? J. Geophys. Res. Atmos. *118*, 4964–4973.

30. Stokes, M.D., Deane, G.B., Prather, K., Bertram, T.H., Ruppel, M.J., Ryder, O.S., Brady, J.M., and Zhao, D. (2013). A marine aerosol reference tank system as a breaking wave analogue for the production of foam and sea-spray aerosols. Atmos. Meas. Tech. *6*, 1085–1094.

31. Wang, X., Sultana, C.M., Trueblood, J., Hill, T.C.J., Malfatti, F., Lee, C., Laskina, O., Moore, K.A., Beall, C.M., McCluskey, C.S., et al. (2015). Microbial control of sea spray aerosol composition: a tale of two blooms. ACS Cent. Sci. *1*, 124–131.

32. Keene, W.C., Maring, H., Maben, J.R., Kieber, D.J., Pszenny, A.A.P., Dahl, E.E., Izaguirre, M.A., Davis, A.J., Long, M.S., Zhou, X., et al. (2007). Chemical and physical characteristics of nascent aerosols produced by bursting bubbles at a model air-sea interface. J. Geophys. Res. Atmos. *112*, 1–16.

33. Granum, E., Kirkvold, S., and Myklestad, S.M. (2002). Cellular and extracellular production of carbohydrates and amino acids by the marine diatom *Skeletonema costatum*: Diel variations

and effects of N depletion. Mar. Ecol. Prog. Ser. *242*, 83–94.

34. Urbani, R., Sist, P., Pletikapić, G., Radić, T.M., Svetličić, V., and Zutic, V. (2012). Diatom polysaccharides: extracellular production, isolation and molecular characterization. In The Complex World of Polysaccharides, D.N. Karunaratne, ed. (InTech). http://dx.doi.org/10.5772/51251.

35. Jayarathne, T., Sultana, C.M., Lee, C., Malfatti, F., Cox, J.L., Pendergraft, M.A., Moore, K.A., Azam, F., Tivanski, A.V., Cappa, C.D., et al. (2016). Enrichment of saccharides and divalent cations in sea spray aerosol during two phytoplankton blooms. Environ. Sci. Technol. *50*, 11511–11520.

36. Cochran, R.E., Laskina, O., Jayarathne, T., Laskin, A., Laskin, J., Lin, P., Sultana, C.M., Lee, C., Moore, K.A., Cappa, C.D., et al. (2016). Analysis of organic anionic surfactants in fine (PM2.5) and coarse (PM10) fractions of freshly emitted sea spray aerosol. Environ. Sci. Technol. *50*, 2477–2486.

37. Hayakawa, K., Handa, N., Kawanobe, K., and Wong, C.S. (1996). Factors controlling the temporal variation of fatty acids in particulate matter during a phytoplankton bloom in a marine mesocosm. Mar. Chem. *52*, 233–244.

38. Jeffrey, L.M. (1966). Lipids in sea water. J. Am. Oil. Chem. Soc. *43*, 211–214.

39. Marty, J.C., Saliot, A., Buat-Ménard, P., Chesselet, R., and Hunter, K.A. (1979). Relationship between the lipid compositions of marine aerosols, the sea surface microlayer, and subsurface water. J. Geophys. Res. Ocean. *84*, 5707.

40. Osterroht, C. (1993). Extraction of dissolved fatty acids from sea water. Fresenius J. Anal. Chem. *345*, 773–779.

41. Slowey, J.F., Jeffrey, L.M., and Hood, D.W. (1962). The fatty-acid content of ocean water. Geochim. Cosmochim. Acta *26*, 607–616.

42. Gagosian, R.B., Peltzer, E.T., and Zafirioui, O.C. (1981). Atmospheric transport of continentally derived lipids to the tropical north Pacific. Nature *291*, 312–314.

43. Ziemann, P.J. (2005). Aerosol products, mechanisms, and kinetics of heterogeneous reactions of ozone with oleic acid in pure and mixed particles. Faraday Discuss. *130*, 469.

44. Marron, A.O., Alston, M.J., Heavens, D., Akam, M., Caccamo, M., Holland, P.W.H., and Walker, G. (2013). A family of diatom-like silicon transporters in the siliceous loricate choanoflagellates. Proc. Biol. Sci. *280*, 20122543.

45. Compiano, A.-M., Romano, J.-C., Garabetian, F., Laborde, P., and de la Giraudièrea, I. (1993). Monosaccharide composition of particulate hydrolysable sugar fraction in surface microlayers from brackish and marine waters. Mar. Chem. *42*, 237–251.

46. Gao, Q., Leck, C., Rauschenberg, C., and Matrai, P.A. (2012). On the chemical dynamics of extracellular polysaccharides in the high arctic surface microlayer. Ocean Sci. *8*, 401–418.

47. van Pinxteren, M., Müller, C., Iinuma, Y., Stolle, C., and Herrmann, H. (2012). Chemical characterization of dissolved organic compounds from coastal sea surface microlayers (Baltic Sea, Germany). Environ. Sci. Technol. *46*, 10455–10462.

48. Cunliffe, M., Engel, A., Frka, S., Gašparović, B., Guitart, C., Murrell, J.C., Salter, M., Stolle, C., Upstill-Goddard, R., and Wurl, O. (2013). Sea surface microlayers: a unified physicochemical and biological perspective of the air–ocean interface. Prog. Oceanogr. *109*, 104–116.

49. Waterkeyn, L., and Bienfait, A. (1987). Localization and function of beta 1,3-glucans (callose and chrysolaminarin) in *Pinnularia* genus (diatoms). Cell *74*, 199–226.

50. Gügi, B., Le Costaouec, T., Burel, C., Lerouge, P., Helbert, W., and Bardor, M. (2015). Diatom-specific oligosaccharide and polysaccharide structures help to unravel biosynthetic capabilities in diatoms. Mar. Drugs *13*, 5993–6018.

51. Aslam, S.N., Cresswell-Maynard, T., Thomas, D.N., and Underwood, G.J.C. (2012). Production and characterization of the intra- and extracellular carbohydrates and polymeric substances (EPS) of three sea-ice diatom species, and evidence for a cryoprotective role for EPS. J. Phycol. *48*, 1494–1509.

52. Meredith, T.C., Aggarwal, P., Mamat, U., Lindner, B., and Woodard, R.W. (2006). Redefining the requisite lipopolysaccharide structure in *Escherichia coli*. ACS Chem. Bol. *1*, 33–42.

53. Boman, H.G., and Monner, D.A. (1975). Characterization of lipopolysaccharides from *Escherichia coli* K-12 mutants. J. Bacteriol. *121*, 455–464.

54. Zarrouk, H., Karibian, D., Bodie, S., Perry, M.B., Richards, J.C., and Caroff, M. (1997). Structural characterization of the lipids a of three *Bordetella bronchiseptica* strains: variability of fatty acid substitution. J. Bacteriol. *179*, 3756–3760.

55. Sforza, S., Silipo, A., Molinaro, A., Marchelli, R., Parrilli, M., and Lanzetta, R. (2004). Determination of fatty acid positions in native lipid a by positive and negative electrospray ionization mass spectrometry. J. Mass Spectrom. *39*, 378–383.

56. Carlson, R.W., Kalembasa, S., Turowski, D., Pachori, P., and Noel, K.D. (1987). Characterization of the lipopolysaccharide from a rhizobium phaseoli mutant that is defective in infection thread development. J. Bacteriol. *169*, 4923–4928.

57. Marvasi, M., Visscher, P.T., and Casillas Martinez, L. (2010). Exopolymeric substances (EPS) from *Bacillus subtilis*: polymers and genes encoding their synthesis. FEMS Microbiol. Lett. *313*, 1–9.

58. Kumar, A.S., Mody, K., and Jha, B. (2007). Bacterial exopolysaccharides - a perception. J. Basic Microb. *47*, 103–117.

59. Morris, H.S., Estillore, A.D., Laskina, O., Grassian, V.H., and Tivanski, A.V. (2016). Quantifying the Hygroscopic Growth of Individual Submicrometer Particles with Atomic Force Microscopy. Anal. Chem. *88*, 3647–3654.

60. Schill, S.R., Collins, D.B., Lee, C., Morris, H.S., Novak, G.A., Prather, K.A., Quinn, P.K., Sultana, C.M., Tivanski, A.V., Zimmermann, K., et al. (2015). The impact of aerosol particle mixing state on the hygroscopicity of sea spray aerosol. ACS Cent. Sci. *1*, 132–141.

61. Petters, M.D., and Kreidenweis, S.M. (2007). A single parameter representation of hygroscopic growth and cloud condensation nucleus activity-part 3: including surfactant partitioning. Atmos. Chem. Phys. *7*, 1081–1091.

Chem, Volume *2*

Supplemental Information

Molecular Diversity of Sea Spray Aerosol Particles: Impact of Ocean Biology on Particle Composition and Hygroscopicity

Richard E. Cochran, Olga Laskina, Jonathan V. Trueblood, Armando D. Estillore, Holly S. Morris, Thilina Jayarathne, Camille M. Sultana, Christopher Lee, Peng Lin, Julia Laskin, Alexander Laskin, Jacqueline A. Dowling, Zhen Qin, Christopher D. Cappa, Timothy H. Bertram, Alexei V. Tivanski, Elizabeth A. Stone, Kimberly A. Prather, and Vicki H. Grassian

SUPPLEMENTAL EXPERIMENTAL PROCEDURES

1. Laboratory Production of Ocean-Relevant SSA

1.1. Oceanic Phytoplankton Bloom

The oceanic phytoplankton bloom was generated in a wave channel located in the Hydraulics Laboratory at Scripps Institution of Oceanography. The CAICE intensive campaign IMPACTS (Investigation into Marine PArticle Chemistry and Transfer Science) was conducted from July 1-August 1, 2014. The experiment has been previously described in detail.[1]

2. Collection of SSA and Seawater During the Mesocosm

2.1. Sea Spray Aerosol Collection

For spectroscopic analysis, individual SSA particles were collected directly from the waveflume at RH ~ 68-76% on quartz coverslips (Ted Pella Inc., part no. 26016) and 400 mesh carbon type B with Formvar transmission electron microscopy (TEM) grids (Ted Pella, Inc., part no. 01814-F), using the fourth and sixth stages of a Micro-Orifice Uniform Deposition Impactor (MOUDI, MSP Corp. Model 110) operating at a flow rate of 30 lpm. Stage four of the MOUDI samplers collected particles with an aerodynamic diameter between 1.8 and 3.2 µm while stage six collected particles between 0.56 and 1 µm. SSA particles were collected from the wave flume headspace for 1 hour. All samples were sealed with PTFE tape and kept at room temperature until analysis.

For quantifying individual fatty acids in the bulk SSA ensemble, SSA was also collected onto pre-cleaned 47 mm quartz fiber filters using the MOUDI sampler. SSA was collected over multiple days within the mesocosm, sampling for approximately 6–9 hours each day. Flow rates were measured before and after sample collection. SSA Samples were then stored at -20 °C until extraction and analysis.

For quantifying individual saccharides in SSA samples were also collected onto Teflon filters (Pall, Life Sciences) using an Andersen dichotomous $PM_{10/2.5}$ sampler (series 241). $PM_{2.5}$ and $PM_{2.5\text{-}10}$ particles were separated by virtual impaction and were collected simultaneously. Total flow through the sampler was operated at 16.67 lpm while the coarse stream flow was maintained at 1.667 lpm. Flow rates were measured before and after sample collection and the average flow rates of the two measurements were used for the sampled air volume calculations. The total sample collection time for each sample ranged between 3–6 hours at ambient temperature and relative humidity (RH; 67−76%) without being dried. Teflon filters were extracted individually for the saccharide analysis (see Section 5.4).

For tentatively identifying organic species using high resolution mass spectrometry SSA samples were collected onto pre-cleaned 37 mm quartz fiber filters (PALL, Port Washington, NY) using a dichotomous sampler (Andersen Instruments, Inc., Thermo Scientific, Waltham, MA). SSA larger than 10 µm in diameter were removed from the sampled air using a PM_{10} cut-off sampling inlet (Model 246b, Andersen Instruments, Inc., Thermo Scientific). SSA were separated within the dichotomous sampler into two size bins, those with wet diameters between 2.5–10 µm (coarse) and those with wet diameters of 2.5 µm and smaller (fine). SSA samples were collected daily throughout the mesocosm experiment, with each sampling time ranging between 3–6 hours. During sampling the relative humidity at the inlet of the sampling line was monitored, and was consistently between 67–76%. Samples collected on quartz fiber filters were composited chronologically (between 4-6 days of samples were combined) to obtain ~20 µgC. Field blanks were collected every five samples by placing pre-cleaned quartz filters into the sampler without any air flow.

3. Single Particle Measurement of the Chemical Composition of SSA

3.1. Chemicals and Standards Used In the Spectroscopic Analysis of Individual SSA Particles

Sodium chloride (≥99%) was purchased from Fisher Scientific. Lipopolysaccharides (LPS) of *Escherichia coli* (*E. coli*) 0111:B4, galactose (Pharmacopeia Reference Standard), arabinose (≥99%), rhamnose (99%), fucose (≥99%), arabitol (≥98%), mannitol (≥98%), sucrose (≥99%), dodecanoic acid (≥98%), tetradecanoic acid (≥99%),

hexadecanoic acid (≥99%), octadecanoic acid (≥99.5%), pentanoic acid (≥99%), hexanoic acid (≥99.5%), heptanoic acid (≥97%), octanoic acid (≥98%), nonanoic acid (≥97%), decanoic acid (≥98%) and 1-docosanol (98%) were purchased from Sigma-Aldrich. Glucose (99%), N-acetylneuraminic (sialic) acid (97%), glucosamine (98%), 1-hexadecanol (98%) were purchased from Alfa Aesar. 1,2-dipalmitoyl-sn-glycero-3-phosphocholine (DPPC) and 1,2-dihexadecanoyl-sn-glycero-3-phosphate (sodium salt) (DPPA) were purchased from Avanti Polar Lipids. All chemicals were used without further purification. Polydimethylsiloxane solution was purchased from Rain-X (ITW Global Brands, Houston, TX, USA). PRO-REEF© Sea Salt was purchased from Tropic Marin (Wartenberg, Germany).

3.2. Generation of Aqueous Aerosol Standards

Aerosol particles were formed by atomizing (TSI Inc., Model 3076) aqueous solutions or suspensions of the standard that were prepared in Optima-grade water (Fisher Scientific). Upon exiting the atomizer, aerosols were passed through a two diffusion dryers in series (TSI Inc., Model 3062) at a flow rate of 1.5 lpm, and the RH of the aerosol stream was reduced to <5%. A quartz disc (Ted Pella Inc., part no. 16001-1) was placed in the path of the aerosol flow after the diffusion dryer for 2-30 min to collect particles for Raman analysis.

3.3. Raman Spectra Collection

Raman spectroscopy was performed using a LabRam HR Evolution Raman spectrometer (Horiba). The spectrometer was equipped with an Olympus BX41 optical microscope with 100X magnification lens. Raman spectra were recorded in the range of 100–4000 cm^{-1}, Raman scattering was performed using a laser operating at 532 nm. Two exposures of 5-10 s each were averaged to obtain the resulting spectrum. The analyzed days were chosen to cover different stages of the two blooms that were observed during the campaign. July 13 is the pre-bloom condition, July 17 is the peak of the first bloom, July 21 is the day between two blooms when chlorophyll-a concentration in seawater decreased to its pre-bloom minimum, July 25-27 are within the peak of the second bloom and July 31 represent the post-bloom condition.

3.4. Types of Organic Compounds Identified in SSA by Raman

For a quantitative comparison of the spectra from SSA with the spectra obtained from the analysis of standards, χ^2 errors between two spectra were determined. The spectral region between 100 and 550 was excluded to avoid discrepancies associated with a broad quartz peak at ca. 400 cm^{-1}. The χ^2 error is the square of the difference between the spectrum of SSA and the spectrum of the standard at a particular Raman shift, summed over a chosen range of Raman shifts (ν_1 to ν_2) and divided by the number of data points (N; includes highly fluorescent and pyrolyzed particles), and can be calculated according to Equation (1):

$$\chi^2 = \frac{\sum_{\nu_1}^{\nu_2}(SSA - Standard)^2}{N}$$

Sodium chloride has no first order vibrational transitions in the 100−4000 cm^{-1} range. The spectrum categorized as chloride salts (Figure 1a) has been assigned based on the lack of vibrational transitions in this region. Figure S1 shows the comparison of spectra of each organic type of SSA spectra with representative members of the class of organics this type belongs to. Additionally, the results of their subtraction using the sodium chloride spectra and enlarged CH stretching regions are shown.

The SSA spectrum categorized as small-chain fatty acids (Figure 1b) has multiple overlapping peaks in the C–H stretching region that results in a very broad characteristic feature between 2850 and 2950 cm^{-1}. These peaks can be assigned to CH_2 symmetric stretching (2853), CH_2 asymmetric stretching (2904 cm^{-1}) and CH_3 symmetric stretching (2927 cm^{-1}). These spectra also show a broad peak at 1068 cm^{-1} due to C-C stretching as well as signatures at 1303 cm^{-1} and 1444 cm^{-1}, that are due to CH_2 twisting and bending modes, respectively.[2–6] This SSA spectrum, with a broad feature in the C-H stretching region, is similar to spectra obtained from the analysis of authentic standard of short

chain fatty acids, as shown in Figures S2 and S3. Spectra of pentanoic (C_5), hexanoic (C_6), heptanoic (C_7), octanoic (C_8), nonanoic (C_9) and decanoic (C_{10}) acids also feature broad peaks in the CH stretching region. The SSA spectrum in Figure 1b has the best overlap with spectra of nonanoic acid (C_9), as indicated by the lowest χ^2 error. This result is consistent with the observation of nonanoic acid (C_9) during analysis of SSA by high resolution mass spectrometry (SI Text, section 5.2).

For the SSA spectrum that is categorized as long-chain fatty acids (Figure 1c), the most prominent peaks were in the C-H stretching region at 2846 cm^{-1} and 2880 cm^{-1}, corresponding to the symmetric and asymmetric stretches of the CH_2 group, respectively. Additional peaks of lower intensity were observed in 1050 to 1500 cm^{-1} region. These Raman modes are associated with the vibration of CH_2 groups (particularly C-C stretching; 1062 cm^{-1}, 1129 cm^{-1}), CH_2 twisting (1295 cm^{-1}) and CH_2 bending (1439 cm^{-1} and 1461 cm^{-1}).[2–5,7] These spectrum were compared with the spectra obtained from the analysis of authentic standard of saturated fatty acids with even-number carbon chain lengths between 12 and 18, fatty alcohols with carbon chain lengths of 16 and 22 as well as with two different species of phospholipids: 1,2-dipalmitoyl-*sn*-glycero-3-phosphate (DPPA) and 1,2-dipalmitoyl-*sn*-glycero-3-phosphocholine (DPPC). Even-chain species were chosen due to their high-prevalence from biological sources in the ocean biota.[8] The results from the comparison between the spectra of the standards and that of the spectra shown in Figure 1c are shown in Figures S4 and S5. Spectra of all standard acids, alcohols and phospholipids are very similar with prominent peaks in the C-H stretching region and lower intensity peaks in 1050 to 1500 cm^{-1} region due to CH_2 group vibrations. Comparison using χ^2 errors (Figure S5) shows a good match between spectra of SSA and the various fatty acid standards. The presence of long-chain fatty acids in the SSA was further supported through the analysis of the SSA from the mesocosm using high resolution mass spectrometry (SI Text, section 5.2). Similar Raman signatures have also been observed in SSA samples collected in the Pacific ocean, which were attributed to long chain organics.[9]

The SSA spectrum categorized as free monosaccharides (Figure 1d) features four peaks in the CH stretching region (2915, 2936, 2985, 2998 cm^{-1}) in addition to a large 3408 cm^{-1} peak due to OH stretching, a peak from the stretching vibration of C-O bond (1097 cm^{-1}), bending deformations of a COH group (867 cm^{-1}), vibration of CH_2 and CH_2OH groups (1310, 1363, 1428, 1452, 1475 cm^{-1}) as well as the vibration of an amide group (amide I band) (1640 cm^{-1}).[2,10–13] The OH stretch at 3275 cm^{-1} may also be due to the overtone of the amide I band. Spectra from Figure 1d has been compared with the spectrum of the aged LPS (aged by storing quartz discs that contained aqueous LPS aerosols for 1 month at 20°C and 17-20% RH) as well as spectra obtained from the analysis of free saccharides representative of marine biology.[14–19] Comparisons between the spectrum of aged LPS and standards of free saccharides are shown in Figures S6 and S7. Most of the model compounds and aged LPS have similar characteristic peaks in C-H stretching region. However, the relative intensities of these peaks vary between the free monosaccharide standards and the SSA spectra, resulting in negative χ^2 values in that region. The best overlap is observed between the spectra of SSA and that of aged LPS (as indicated by the lowest χ^2 error). However, the difference in relative intensities of the ring (1000-1100 cm^{-1}) and C-H (2900-3000 cm^{-1}) stretching vibrations are different in SSA and aged LPS, leading to larger χ^2 errors in these regions. Comparisons between the other free saccharide standards show similar discrepancies, with the ratio of intensities of the ring (1000-1100 cm^{-1}) and C-H stretching vibrations (2900-3000) being higher in SSA. Additionally, the OH stretch vibration in SSA is higher and broader than in the free saccharide standards. However, this can be related to water within the SSA particles that gives an overlap of OH vibration of water and structural OH vibration. Peaks at 1009 cm^{-1} and 1037 cm^{-1} in SSA that are not present in the spectra of model saccharides, resulting in positive χ^2 values in that region, are associated with sulfates (indicated in Figure S7), with 1009 cm^{-1} corresponding to SO_4^{2-} and 1037 cm^{-1} to HSO_4^- symmetric stretches, respectively.[20,21] The hydroxyl groups of saccharides can be substituted with sulfate groups. Based on these comparisons, the SSA shown in Figure 1d can be associated with aged LPS or with a mixture of free saccharides. Better overlap of the SSA shown in Figure 1d can be achieved by mixing representative free saccharides. A mixture (denoted in Figures S6 and S7 as "Mix of Saccharides") consisting of 40% fructose, 40% sucrose, 15% arabitol and 10% glucose (mixed computationally) gives the lowest χ^2 error and better overlaps with spectra of SSA shown in Figure 1d.

The SSA spectrum categorized as siliceous material (Figure 1e) has a peak at 791 cm^{-1} corresponding to a Si-C asymmetric stretching mode. Additional peaks at 862, 1260, and 1408 cm^{-1} correspond to rocking as well as symmetric and asymmetric bending of CH_3 groups, respectively.[22] This spectrum has been compared to the spectra of a diatom

collected from a marine biofilm as well as a hydrophobic coating containing polydimethylsiloxane (PDMS) as a main component (Figure S9). The siliceous material of diatoms has been found to incorporate a framework of SiO_2 polymer structures along with polysaccharides.[23] All three spectra (of SSA, diatom and PDMS) exhibit two large peaks at 2906 and 2967 cm^{-1}. The relative intensities for these two Raman modes are slightly different between the spectra, resulting in a positive χ^2 error at 2906 cm^{-1}. The peaks in the 550-1500 cm^{-1} region overlap well, leading to a subtraction spectrum close to that of quartz (quartz signature is present due to a low signal of a diatom). Diatoms are known to have rigid cell walls (frustules) composed of amorphous silica (SiO_2) which is released upon cell lysis.[24,25]

The SSA spectrum categorized as polysaccharides (Figure 1f) features skeletal C-C, C-O and stretching C-C-O bands at 991 and 1044 cm^{-1}, CH_2 bending vibration that typically appears at 1459 cm^{-1} in lipids, a peak at 1642 cm^{-1} that can be either C=O stretching in carbohydrates or C=C stretching vibration of unsaturated fatty acid chains and a broad peak at 2929 cm^{-1} identified as the C–H stretching modes of -CH-, methylene (-CH_2-) and terminal methyl (-CH_3) groups of fatty acid chains.[26,27] This spectrum obtained from SSA was compared with the spectrum of commercially available standards representative of cellular polysaccharides: lipopolysaccharide (LPS) from *E. coli*, lamanarin, inulin, sodium alginate and peptidoglycan. For a quantitative comparison of the spectra from SSA with the spectra obtained from the standards of cellular polysaccharides, χ^2 errors between two spectra were determined for the 550–4000 cm^{-1} spectral range (see Figure S8).

As can be seen in the χ^2 errors shown in Figure S8, the spectra of *E. coli* LPS features similarly shaped broad peak in C-H stretching region that is only slightly shifted from that of the SSA spectrum, resulting in a slight deviation in the subtraction spectrum around the baseline. Low χ^2 error (~0.01 for spectra normalized at 1) indicates a good match between the spectra of SSA and LPS of *E. coli*. Figure S8 also shows a good fit between the spectra of SSA and sodium alginate. It is well known that diatoms exude adhesive polymers similar to sodium alginate in order to adhere to surfaces that are polysaccharides cross-linked via O-glycosidic sugar-protein linkages into large proteoglycan assemblages.[28] Therefore it can be proposed that diatoms exude adhesive polysaccharide polymers (extracellular polymeric substances, EPS) to adhere to the walls of the wave channel, and are then transferred to the water and then eventually to the aerosol phase. In the mesocosm experiment described in this paper, the walls of the wave channel are the most important surfaces. In the open ocean, micelles, gels and colloids formed at high concentrations can provide adsorption surfaces for other dissolved organic matter.[29–31] Due to the similarities between the spectra of the cellular polysaccharide standards, it is difficult to explicitly indicate the specific polysaccharide species present in the SSA. However, dissimilarities exist between the spectra of known polysaccharides and those of a mixture of free saccharides (Figure S6).

3.5. Determining the External Mixing State of Individual Particles within the SSA Population

Using comparisons to authentic standards, the individual particles of the SSA population collected during the mesocosm were analyzed using Raman analysis and classified as either aliphatic-rich (AR) or oxygen-rich (OR). The SS-OC categories containing organic species with low O:C values (<0.2) (i.e., long-chain fatty acids) were classified as AR, while those with O:C values ≥0.2 (i.e., free saccharides, polysaccharides, siliceous material and short-chain fatty acids) were considered as OR. The number fraction (F_j) of the individual particles of the population of SSA particles analyzed that exhibited each of these characteristics was calculated using Equations 2 & 3:

$$F_{AR} = \frac{N_{AR}}{N_{Total}} \quad (2)$$

$$F_{OR} = \frac{N_{OR}}{N_{Total}} \quad (3)$$

where N_{AR} and N_{OR} are the total number of particles assigned to the aliphatic-rich and oxygen-rich classifications, respectively.

4. Measuring Climate-Relevant Properties of SSA

4.1. Hygroscopic Growth Measurements of Individual Substrate Deposited Nascent SSA Particles by Atomic Force Microscopy

A molecular force probe 3D AFM (Asylum Research, Santa Barbara, CA) was used for water uptake studies at 298 K. Hydrophobically coated silicon wafers containing substrate deposited particles were placed in an AFM humidity cell setup, which is described elsewhere [32]. Images were collected in AC mode with silicon nitride AFM probes (MikroMasch, Model CSC37) with a nominal spring constant of 0.35 N/m and a typical tip radius of curvature of 10 nm. For quantifying water uptake at a specific RH, images were taken at low RH (<5%) followed by images at higher RH (60% and 80%), allowing at least 15−20 min equilibration time for water uptake at both 60% and 80% RH. The free amplitude and set point used for imaging the liquid particles at high RH were relatively large (3−5 V) to achieve optimal imaging without moving or breaking the droplets. Scan rates were between 1.0−1.3 Hz. Repeated imaging of the sample area at high RH can be problematic and the data were obtained using the least amount of imaging possible. It should be noted that similar measured GF values have been obtained using both AFM (area GF) and HTDMA (volume GF).[32] Discrepancies between GF values determined by AFM and HTDMA may arise from substrate hydrophobicity and particle deformation due to substrate impaction.[32]

4.2. Hygroscopic Growth Measurements of Bulk Aerosol Mimics by Hygroscopic Tandem Differential Mobility Analyzer (HTDMA)

HTDMA measurements of the hygroscopic growth of 100 nm particles were performed using a Multi-Analysis Aerosol Reactor System (MAARS). The procedure has been reported previously (see Ref. 72 of main text) and therefore in-depth details will not be covered here. Briefly, aerosol particles were generated by atomizing a ~0.1 % wt solution of the aerosol mimics containing either glucose (Sigma-Aldrich); sodium alginate (Sigma-Aldrich, ≥99.5%), LPS (Sigma-Aldrich), nonanoic acid (≥97%) or palmitic acid (≥99%) all as 1:2 or 1:1 mixtures (palmitic acid mixture was a saturated solution) with NaCl (Fisher Scientific, 99%). A mono-disperse dry particle (RH <5%) of diameter D_0 is selected by the first differential mobility analyzer (DMA1) and then sent to the hydration chamber where they are equilibrated to a defined relative humidity (RH). Upon exiting the hydration chamber, the humidified particles are sent to the second DMA (DMA2) coupled with ultrafine condensation particle counter (UCPC) where the humidified mobility diameter is measured, Dp. The growth factor (GF) at each RH was calculated Equation 4, based on the ratio of the humidified diameter to the dry diameter of the particles in the ensemble:

$$GF = \frac{D_p(RH)}{D_0} \tag{4}$$

The κ value was calculated from the GF measurements summarized below following Petters and Kreidenweis [33].

$$\kappa = \frac{GF^3 - 1}{RH/100} \exp\left[\frac{A}{D_o \cdot GF}\right] - \left(GF^3 - 1\right) \tag{5}$$

where D is the wet particle diameter and A is calculated from:

$$A = \frac{4\sigma M_w}{RT\rho_w} \tag{6}$$

where σ is the surface tension of water (0.072 J/m^2) M_w is the molecular weight of water (0.018 kg/mol), and ρ_w is the density of water (1000 kg/m^3) at 298K.

5. Measurements of the Chemical Composition of Bulk SSA Populations

5.1. Quantifying the Total Organic Carbon Content of SSA

The total organic carbon (TOC) content of SSA collected onto quartz fiber filters using the MOUDI sampler was measured using a thermal optical analyzer (Sunset Laboratories) following the ACE-Asia protocol, using laser reflectance to monitor carbon pyrolysis. The concentration of TOC in bulk SSA was calculated using Equation (7):

$$[TOC]_{SSA} = \frac{m_{filter}^{TOC}}{V_{air}} \quad (7)$$

where $[TOC]_{SSA}$ is the concentration of TOC in the SSA (in ng/m^3), m^{TOC}_{filter} is the total mass of TOC on the quartz fiber filter, and V_{air} is the total volume of air sampled from the headspace of the waveflume chamber.

5.2. Electrospray Ionization High Resolution Mass Spectrometry

Details on analysis of SSA samples for identifying organic compounds via empirical formula assignments can be found in Reference [34]. Briefly, SSA samples from the mesocosm experiment were analyzed using an electrospray-linear ion trap-Orbitrap mass spectrometer (ESI-LIT-Orbitrap) (LTQ Orbitrap XL, Thermo Fisher, Bremen, Germany) located at the Environmental Molecular Sciences Laboratory (Richland, Washington). Samples were introduced to the ESI-LIT-Orbitrap MS by direct infusion. The ESI source was operated in the negative ion mode with a capillary voltage of 4 kV. Empirical formulas were assigned to each major peak in the MS spectra using formula calculation software. Calculations were performed using element ranges of ^{12}C: 0–50, ^{1}H: 0–100, ^{16}O: 0–10, ^{14}N: 0–10, ^{32}S: 0–2, ^{31}P: 0–2, ^{35}Cl: 0–1 and ^{13}C:0–1 with a mass tolerance of 2 ppm. In addition a limit of 10 for the double-bond equivalency (DBE) was used. In negative mode, all assigned masses were for the deprotonated molecular ion ([M–H]$^-$), with little to no Cl^- adducts observed. None of the assigned masses resulted from chlorine adducts. All HRMS responses in the samples were subtracted by those measured in field blanks.

5.3. Quantification of C_4–C_{20} Fatty Acids in Size-Resolved SSA

SSA samples collected onto quartz fiber filters using the MOUDI sampler were extracted sequentially by sonication using four separate volumes of 5 mL of dichloromethane. Authentic deuterium-labelled standards of C_{10} (decanoic acid-d_{19}), C_{14} (tetradecanoic acid-d_{27}), C_{17} (heptadecanoic acid-d_{33}) and C_{20} (eicosanoic acid-d_{39}) saturated fatty acids were used as internal standards and spiked directly to the filter immediately prior to the addition of solvent and sonication extraction. The final combined extract volume of 20 mL was reduced to 200 µL under a gentle stream of nitrogen at room temperature. A 1 µL aliquot of the final extract volume was analyzed by gas chromatography-mass spectrometry (GC-MS). GC-MS analysis was performed using a Stabilwax-DA column (Restek, Bellefonte, PA, USA) and an oven temperature program with the following steps: 40 °C for 2 min, followed by a ramp at 10 °C/min to 250 °C, then switched to a ramp at 5 °C/min until 280 °C, then held at 250 °C for 5 min. A split/splitless injector was used at 280 °C, running in pulsed splitless mode with a splitless time of 0.95 min. The carrier gas flow through the column was maintained at 1.0 mL/min. The GC-MS transfer line was maintained at 280 °C throughout the entire run. MS data was acquired in both total ion current (TIC; *m/z* 50–500) and selected ion monitoring (SIM) modes simultaneously. For SIM, the $[C_2H_4O_2]^{+\bullet}$ (*m/z* 60) product ion resulting from the McLafferty rearrangement of the parent molecular ion ($[M]^{+\bullet}$) was monitored for each saturated fatty acid compound. All quantitation of fatty acids was performed using the SIM data, with calibration curves created from the analysis of a mixture of authentic standards of C_4–C_{20} even-carbon saturated fatty acids as well as C_{16} and C_{18} mono- and poly-unsaturated fatty acids. The identification of fatty acids was supported through the matching of GC-MS retention times observed in SSA samples to those of authentic standards and matching observed TIC spectra to those in a MS spectral database (NIST MS Search version 2.0f, 2009).

The calculation of fatty acid concentrations in bulk SSA was performed using Equation (8):

$$[FA]_{i,SSA} = \frac{([FA]_{i,extract} - [FA]_{i,blank}) \times V_{extract}}{V_{air}} \quad (8)$$

where $[FA]_{SSA}$ is the concentration of fatty acid *i* in the bulk SSA (in ng/m^3). $[FA]_{i,extract}$ and $[FA]_{i,blank}$ are the concentrations of fatty acid *i* in the final extract and field blank, respectively, as analyzed by GC-MS (in ng/mL). $V_{extract}$ is the final volume of the extract analyzed by GC-MS (in mL) and V_{air} is the total volume of air sampled from the headspace of the waveflume chamber (m^3).

5.4. Quantification of Saccharides in Size-Resolved SSA

Teflon filters containing SSA were wetted by 200 µL of acetone and then extracted into 6.00 mL of ultra-pure water by 10 minute shaking (125 rpm, VWR) and 30 minute ultra-sonication (60 sonics min^{-1}, 5510-Branson) at room temperature. An aliquot was taken out for free monosaccharide analysis and rest of the extraction was mildly hydrolyzed using TFA (trifluoroacetic acid) at a final concentration of 0.1 M at 100℃ for 12 hours.[35]

Instrumental analysis was conducted using ion chromatography (Dionex-ICS 5000) along with electrochemical detector (ED) that equipped with a Dionex CarboPac™ PA20 (3 × 150 mm, product # 060142) carbohydrate column, corresponding guard column, and Dionex AminoTrap™ trap column. The mobile phase consisted of 27.5 mM aqueous sodium hydroxide, which was prepared with degassed ultra-pure water and stored under pressurized (30 psi) ultra-pure nitrogen environment. Isocratic elution was performed at a 0.480 mL min^{-1} flow rate and, column cleanup and regeneration was performed before each injection using 200 mM sodium hydroxide at the same flow rate over 15 minutes. A constant temperature of 30℃ was maintained in both column and detector compartments. A DV-50 (Dionex) auto sampler and a 25 µL injection loop were used for sample injection. Peak identification of the individual saccharides was performed based on the retention times of 15 different saccharide authentic standards. (xylitol, mannitol, arabinose, glucose, xylose, fructose (Sigma-Aldrich), erythritol, arabitol, trehalose, fucose, (Alfa-Aesar), rhamnose, mannose, ribose (Acros Organics), galactose, sucrose (Fisher)). Seven-point calibration curves ranging from 10 nM to 10 µM and based on peak area were used for quantification the saccharides in SSA. The concentrations (in ng/m^3) of all the detected individual saccharides were calculated using the saccharide concentration in the extract, extraction volume and sampled air volume. The sum of the individual saccharides are reported as the total saccharides and used for calculate the total saccharide fraction of TOC.

5.5. Quantification of Inorganic Cation and Anions in Size-Resolved SSA

One eighth of a quartz fiber filter sampled by MOUDI sampler was extracted into 5.00 mL of ultra-pure water (18.2 MΩ resistivity) by shaking (125 rpm) for 12 hours. The extracts were filtered by 0.45 µm PTFE filter and were directly analyzed for water soluble inorganic ions by ion-exchange chromatography coupled with conductivity detection (Dionex, ICS-5000) as described in detail elsewhere.[36] The mass concentration of inorganic ions in SSA (in µg/m^3), were calculated using total filter area and total volume of air sampled from the headspace of the waveflume.

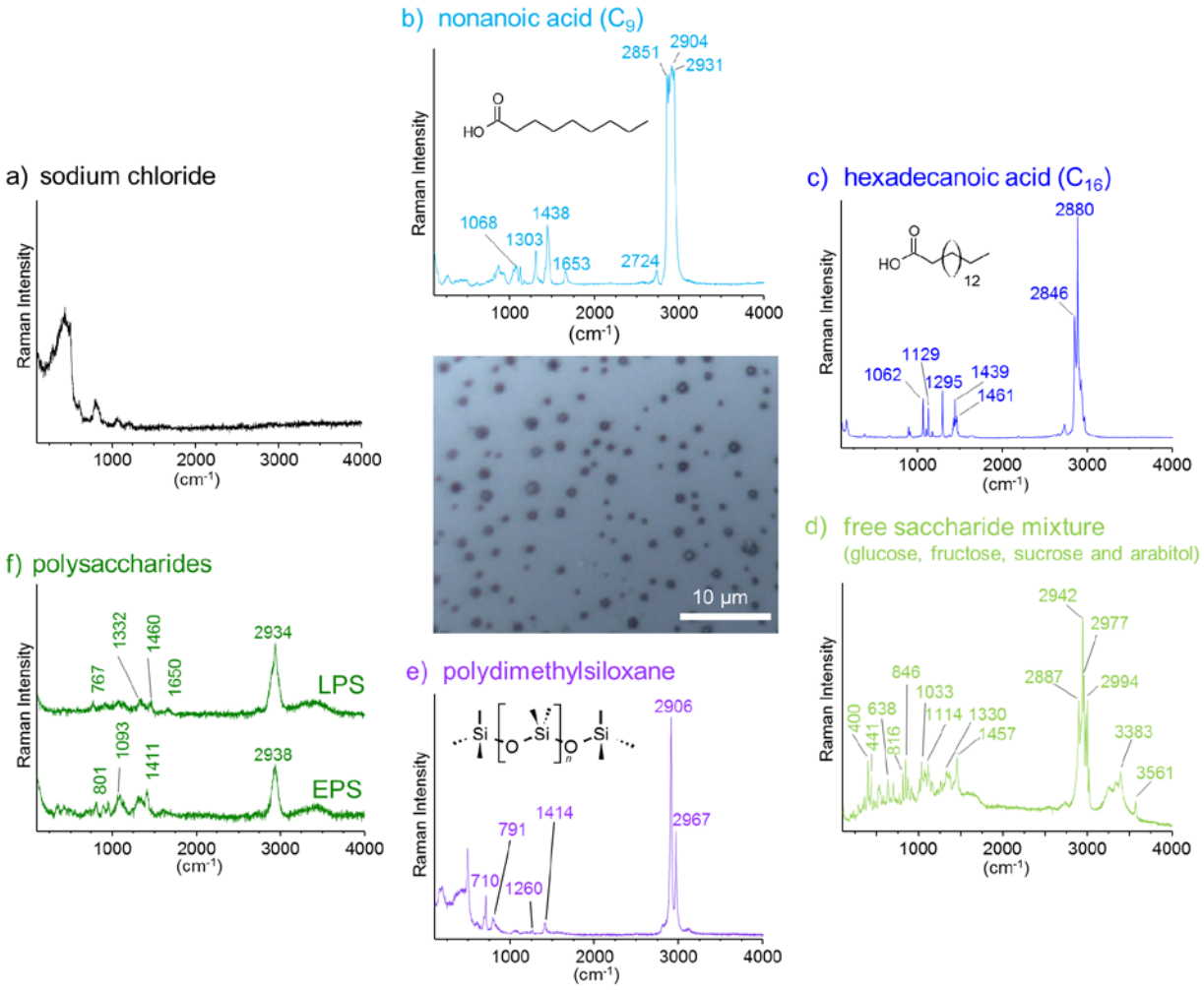

Figure S1. Raman Spectra of Representative Authentic Standards: Direct Relationship to SSA Particles in Figure 1. Related to Figures 1 and 2.

Raman spectra of representative authentic standards from from different classes of organics that closely resemble the spectra observed from individual SSA particles collected during the mesocosm shown in Figure 1 of the main text. Each spectra was recorded from a single particle collected during the atomization of aqueous solutions containing the authentic organic standard, averaging two separate exposures at 5–10 s each. Spectra were recorded in the range of 100–4000 cm^{-1}.

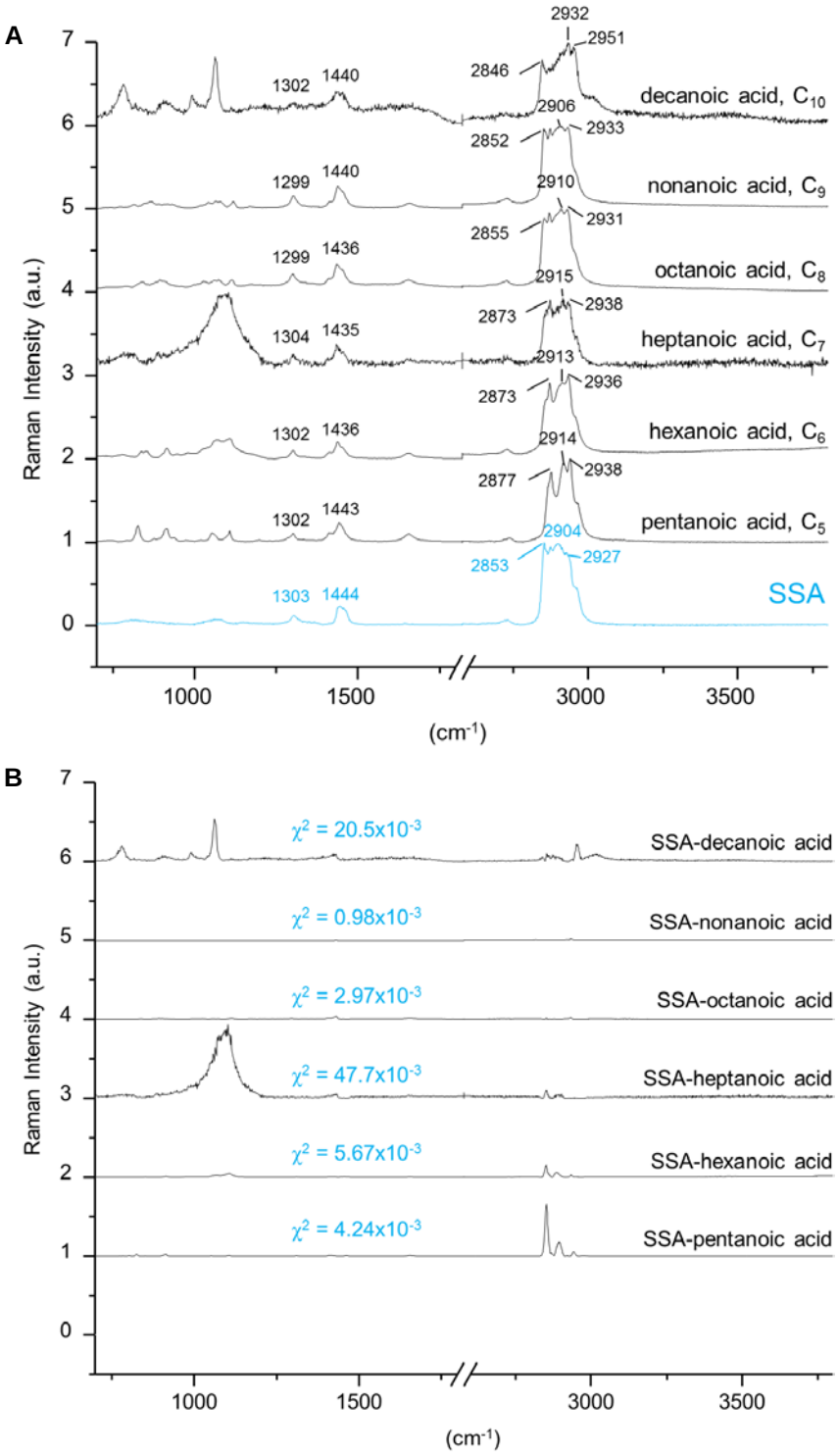

Figure S2. Raman Spectra Obtained for Standards of Short-Chain Saturated Fatty Acids with Statisitical Comparisons to an SSA Particle. Related to Figures 1 and 2

(A) Spectra obtained from a single SSA particle collected during the mesocosm that is proposed to contain a significant fraction of small-chain fatty acids is shown for reference (same spectra shown in Figure 1B of the main text). (B) χ^2 plots showing the statistical relationship between each standard spectra of small-chain saturated fatty acids to that of the single SSA particle collected during the mesocosm (shown in Figure S2A and Figure 1B).

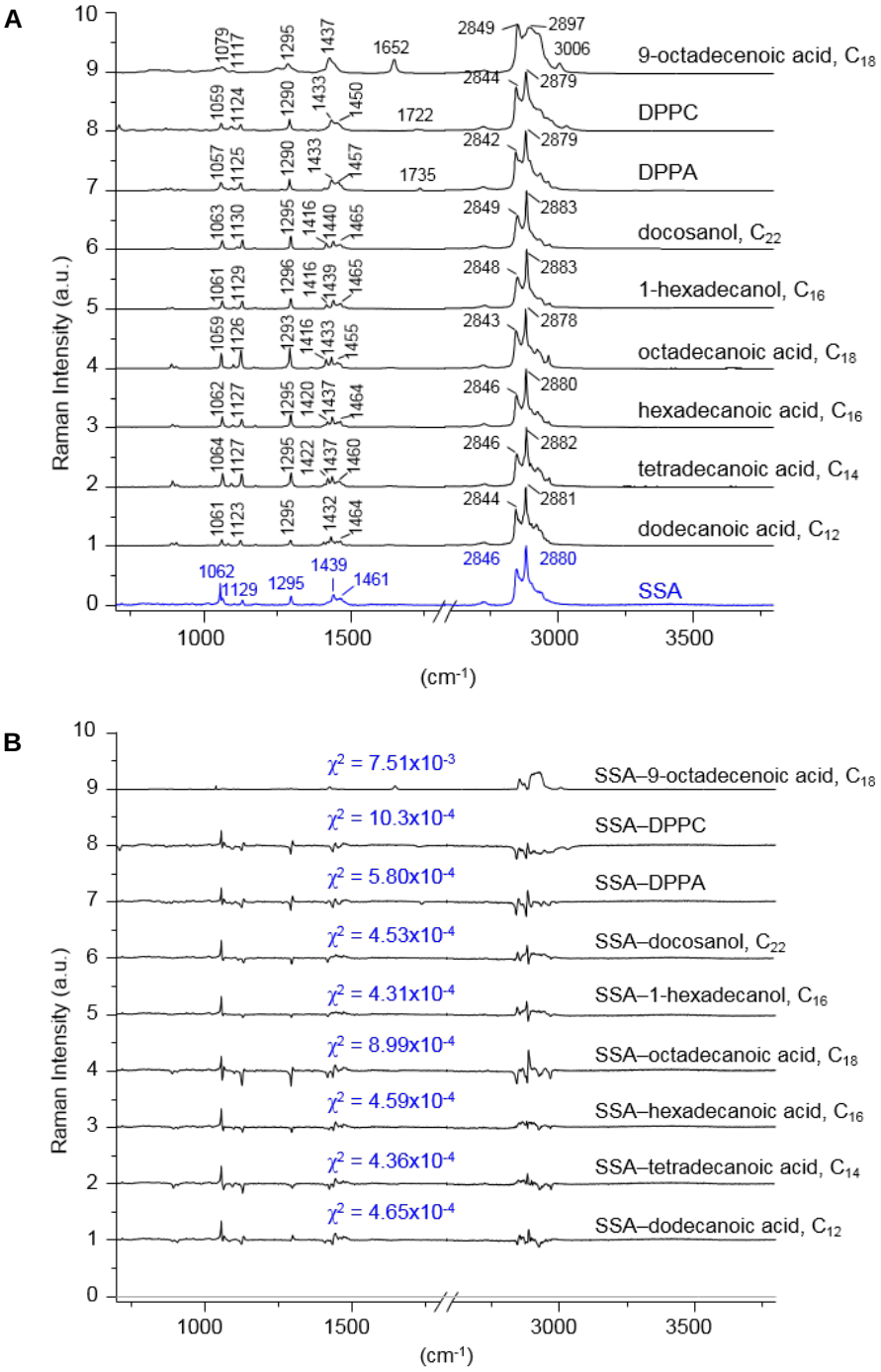

Figure S3. Raman Spectra Obtained for Standards of Long-chain Saturated and Unsaturated Fatty Acids, Linear Alkyl Alcohols, and Phospholipids with Statistical Comparisons to an SSA Particle Classified as "Long-Chain Fatty Acids". Related to Figures 1 and 2

(A) Phospholipids containing hexadecanoic acid ester chains (1,2-dipalmitoyl-sn-glycero-3-phosphatidic acid, DDPA; 1,2-dipalmitoyl-sn-glycero-3-phosphocholine, DPPC). Spectra obtained from a single SSA particle collected during the mesocosm that is proposed to contain a significant fraction of long-chain saturated fatty acids is shown for reference (same spectra shown in Figure 1C of the main text). (B) χ^2 plots showing the statistical relationship between each standard spectra of long-chain saturated fatty acids and alcohols and phospholipids to that of the single SSA particle collected during the mesocosm (shown in Figure S3A and Figure 1C).

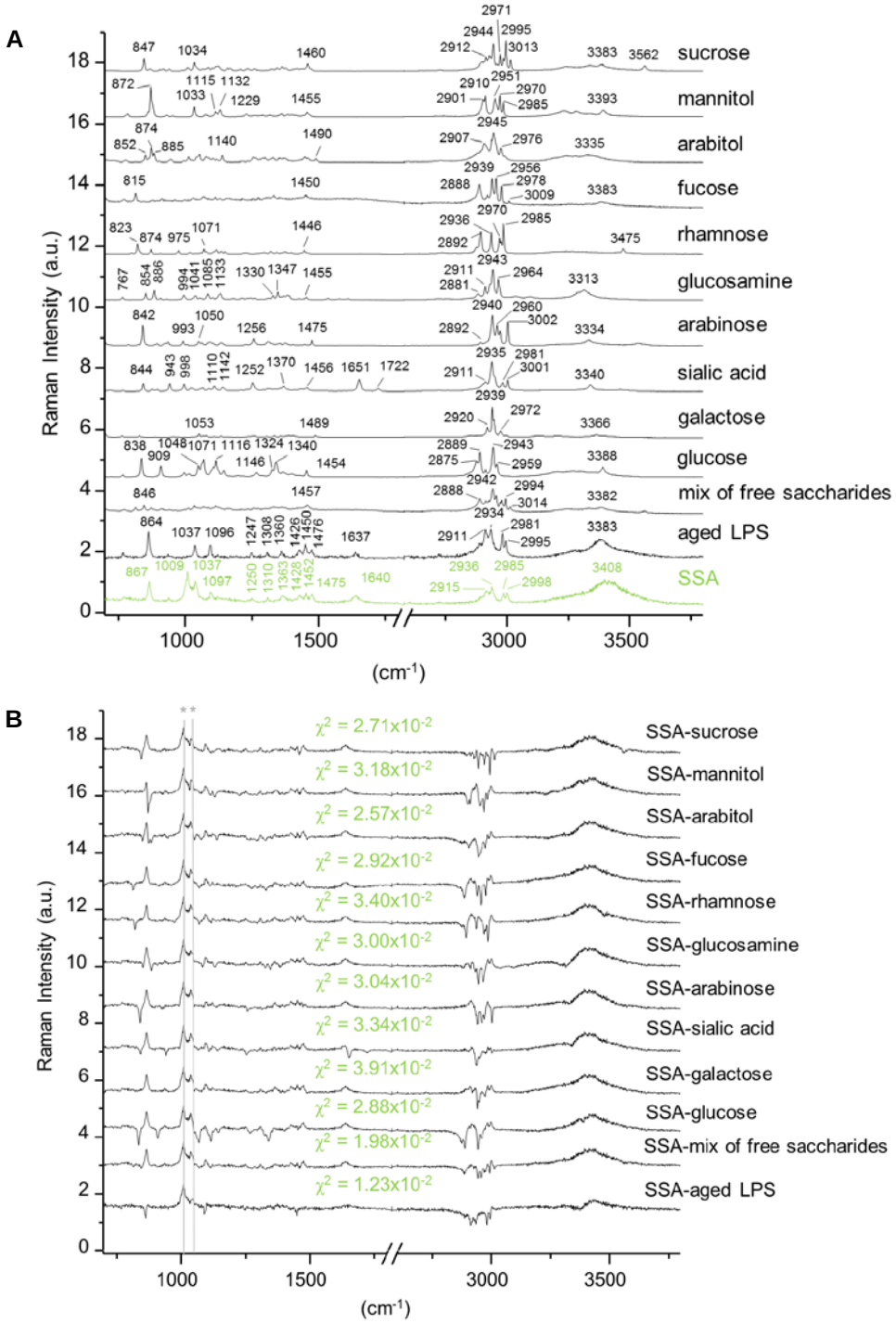

Figure S4. **Raman Spectra Obtained for Standards of Free Saccharides with Statistical Comparisons to an SSA Particle. Related to Figures 1 and 2**

(A) Spectra obtained from a single SSA particle collected during the mesocosm that is proposed to contain a significant fraction of saccharides is shown for reference (same spectra shown in Figure 1d of the main text). The mixture of saccharides (denoted as "Mix of Saccharides") consisted of 40% fucose, 40% sucrose, 15% arabitol and 5% glucose (mixed computationally). (B) χ^2 plots showing the statistical relationship between each standard spectra of free saccharides to that of the single SSA particle collected during the mesocosm (shown in Figure S4A and Figure 1D). Signatures labelled with "*" are due to sulfate signatures present in the SSA spectra.

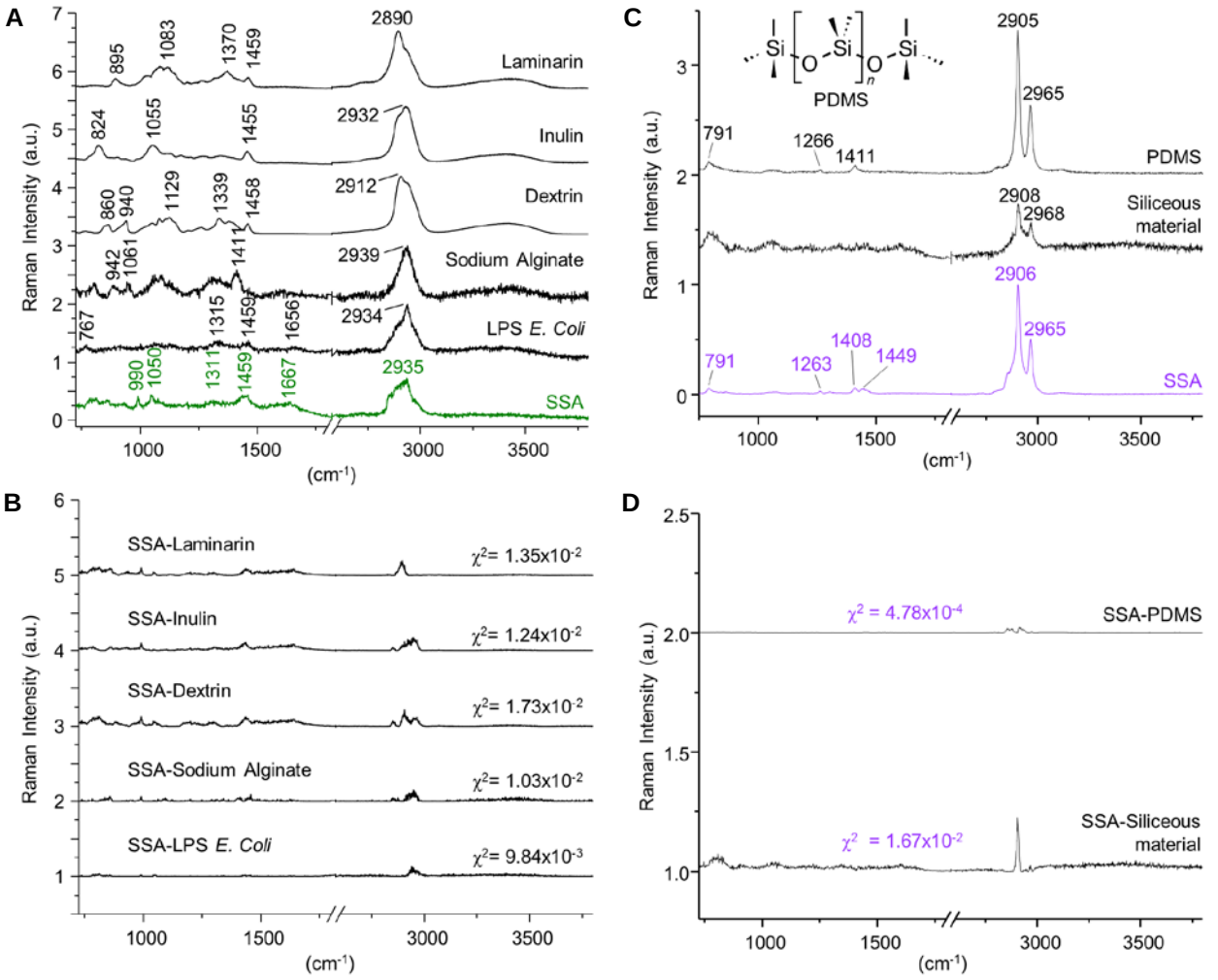

Figure S5. Raman Spectra of Individual Standards of Polysaccharides, Lipopolysaccharide (LPS; from *Escherichia coli* bacteria), PDMS and Siliceous Material and SSA particles with Statistical Comparisons Between Standard Spectra and SSA Particles. Related to Figures 1 and 2

(A) Single particle from SSA in (a) was collected during the mesocosm, with Raman spectra resembling that of polysaccharides (Figure 1F). (B) χ^2 plot shows the statistical relationship between the standard spectra of LPS and sodium alginate to that of the single SSA particle collected during the mesocosm (shown in Figure S5A and Figure 1F). (C) Raman spectra for "Siliceous material" was obtained from the analysis of biofilm collected from the mesocosm. The "SSA" spectra was obtained from a single particle from SSA collected during the mesocosm with Raman spectra resembling that of siliceous material (Figure 1e). (D) χ^2 plots show the statistical relationship between either the standard spectra of PDMS or the biofilm and that of the single SSA particle collected during the mesocosm (shown in Figure S5C and Figure 1E).

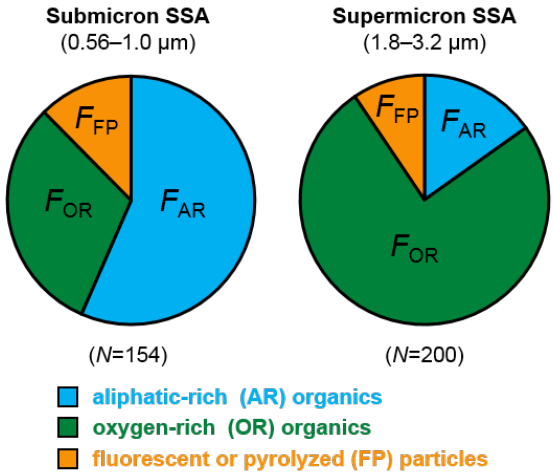

Figure S6. **Number Fraction (F_j) of Individual Particles of SSA (a) Exhibiting Raman Signatures of Aliphatic-rich (F_{AR}) and Oxygen-rich (F_{OR}) Organic Molecules. Related to Figure 1 & 2**

Individual particles of SSA were analyzed by Raman and collected on July 13 and 17 during the first phytoplankton bloom of the mesocosm. F_{FP} are particles that were highly fluorescent or were pyrolyzed during Raman analysis.

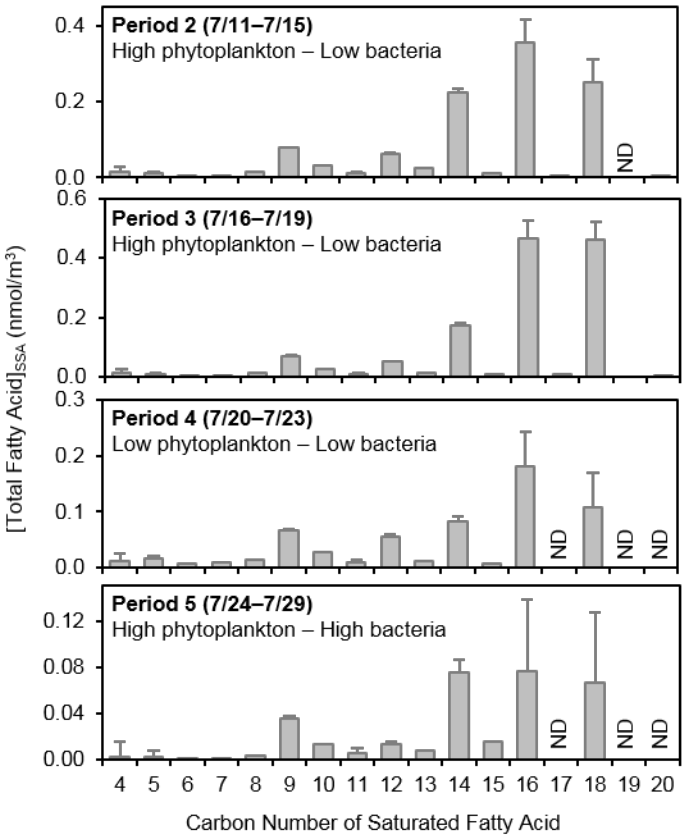

Figure S7. Relative Distribution of Saturated Fatty Acids Quantified in SSA.

See method details in SI Text, section 5.3. Size-resolved SSA was collected during separate periods of the mesocosm experiment, (the duration of collection are shown in the title of each graph). Phytoplankton levels in the seawater were estimated based on chlorophyll-a measurements while bacteria levels in seawater were determined through microscopic techniques.

Table S1. **Number of individual particles within the SSA ensemble collected during selected days of the mesocosm that were analyzed by Raman spectroscopy. Related to Figures 1 and 2**

Based on the number of particles observed on each of the MOUDI stages used in this study, the sample size required to obtain an accurate representation of the bulk ensemble of particles at the 85%, 90% and 95% confidence levels are 23, 96 and 384 particles, respectively.

1.8 – 3.2 µm		560 – 1000 nm	
Date	**Particles Analyzed**	**Date**	**Particles Analyzed**
July 13	149	July 13	120
July 17	200	July 17	154
July 21	121	July 21	118
July 27	72	July 26	123
August 1	192	August 1	65

Table S2. Vibrational assignment of Raman peaks for different molecular components within individual SSA particles (See Ref. 1–3). **Related to Figure 1–2 and S1–S5**

Raman Frequency Shift (cm^{-1})	Vibrational Mode
	Short-Chain Fatty Acids [3]
1068	ν(CC) aliphatic chain vibrations
1303	CH_2 wag
1444	$\delta(CH_2)$ asymmetric bend $\delta(CH_3)$ asymmetric bend
2724	overtone and combination
2853	CH_2 symmetric stretch
2904	CH_2 asymmetric stretch
2927	CH_3 symmetric stretch
	Long-Chain Fatty Acids [3]
1062	ν(C-O) stretch
1129	ν(C-C) stretch
1295	$\delta(CH_2)$ bend
1439-1461	$\delta(CH_2)$ and $\delta(CH_2OH)$ deformations
2723	overtone
2846-2880	ν(C-H)
	Polysaccharides [2]
991	ν(C-O-C) asym
1044	ν(CC) aliphatic chain vibrations
1459	$\delta(CH_2)$ $\delta(CH_3)$ asym
1642	ν(C=O) and amide III
2929	ν(C-H)
	Free Saccharides [2]
861	δ(COH), δ(CCH), δ(OCH) side group deformations
1009 1037 1097	ν(C-O) and ν(C-C) stretches
1310	amide I
1250 1310 1363 1428 1452 1475	$\delta(CH_2OH)$ deformations
1640	ν(C=O), ν(C=C) and amide III
2915	C-H asymmetric stretch
2936 2985 2998	CH_3 symmetric stretch
3408	ν(O-H)
	Polydimethylsiloxane [37]
710	Si-C sym. stretch
791	CH_3 asymmetric rock, Si-C asymmetric stretch
1260	CH_3 symmetric bend
1408	CH_3 asymmetric bend Olefinic CH_2 bend
1449	$\delta(CH_2)$ and $\delta(CH_3)$ asymmetric bend
2906	CH_3 symmetric stretch
2967	CH_3 asymmetric stretch

Table S3. **Number of individual particles within the SSA ensemble collected during selected days of the mesocosm that were analyzed by atomic force microscopy to measure their hygroscopic growth. Related to Figure 2.**

Based on the number of particles observed on each of the MOUDI stages used in this study, the sample size required to obtain an accurate representation of the bulk ensemble of particles at the 85%, 90% and 95% confidence levels are 23, 96 and 384 particles, respectively.

> 1 µm		**0.5 – 1.0 µm**	
Date	**Particles Analyzed**	**Date**	**Particles Analyzed**
July 13	10	July 13	36
July 17	23	July 17	45
July 21	24	July 21	27

References

(1) Wang, X.; Sultana, C. M.; Trueblood, J.; Hill, T. C. J.; Malfatti, F.; Lee, C.; Laskina, O.; Moore, K. A.; Beall, C. M.; McCluskey, C. S.; et al. Microbial Control of Sea Spray Aerosol Composition: A Tale of Two Blooms. *ACS Cent. Sci.* **2015**, *1* (3), 124–131.

(2) Gelder, J. De; Gussem, K. De; Vandenabeele, P.; Moens, L. Reference Database of Raman Spectra of Biological Molecules. *J. Raman. Spectrosc.* **2007**, *38*, 1133–1147.

(3) Hill, I. R.; Levin, I. W. Vibrational Spectra and Carbon–Hydrogen Stretching Mode Assignments for a Series of N-Alkyl Carboxylic Acids. *J. Chem. Phys.* **1979**, *70* (2), 842–851.

(4) Gomes, H.; Rosina, P.; Holakooei, P.; Solomon, T.; Vaccaro, C. Identification of Pigments Used in Rock Art Paintings in Gode Roriso-Ethiopia Using Micro-Raman Spectroscopy. *J. Archaeol. Sci.* **2013**, *40* (11), 4073–4082.

(5) Spiker Jr., R. C.; Levin, I. W. Raman Spectra and Vibrational Assignments for Dipalmitoyl Phosphatidylcholine and Structurally Related Molecules. *Biochim. Biophys. Acta/Lipids Lipid Metab.* **1975**, *388* (3), 361–373.

(6) Haggerty, J. A.; Fisher, J. B. Short-Chain Organic Acids in Interstitial Waters From Mariana and Bonin Forearc Serpentines: Leg 125. *Proc. Ocean Drill. Progr.* **1992**, *125*, 387–395.

(7) Pemberton, J. E.; Chamberlain, J. R. Raman Spectroscopy of Model Membrane Monolayers of Dipalmitoylphosphatidic Acid at the Air-Water Interface Using Surface Enhancement from Buoyant Thin Silver Films. *Biopolymers* **2000**, *57* (2), 103–116.

(8) Mochida, M.; Kitamori, Y.; Kawamura, K.; Nojiri, Y.; Suzuki, K. Fatty Acids in the Marine Atmosphere: Factors Governing Their Concentrations and Evaluation of Organic Films on Sea-Salt Particles. *J. Geophys. Res. Atmos.* **2002**, *107*, 4325.

(9) Deng, C.; Brooks, S. D.; Vidaurre, G.; Thornton, D. C. O. Using Raman Microspectroscopy to Determine Chemical Composition and Mixing State of Airborne Marine Aerosols over the Pacific Ocean. *Aerosol Sci. Technol.* **2014**, *48* (2), 193–206.

(10) She, C. Y.; Dinh, N. D.; Tu, A. T. Laser Raman Scattering of Glucosamine, N-Acetylglucosamine, and Glucoronic Acid. *Biochim. Biophys. Acta* **1974**, *372*, 345–357.

(11) Wu, H.; Volponi, J. V; Oliver, A. E.; Parikh, A. N.; Simmons, B. A.; Singh, S. In Vivo Lipidomics Using Single-Cell Raman Spectroscopy. *Proc. Natl. Acad. Sci. U. S. A.* **2011**, *108* (9), 3809–3814.

(12) Amharref, N.; Beljebbar, A.; Dukic, S.; Venteo, L.; Schneider, L.; Pluot, M.; Manfait, M. Discriminating Healthy From Tumor and Necrosis Tissue in Rat Brain Tissue Samples by Raman Spectral Imaging. *Biochim. Biophys. Acta* **2007**, *1768* (10), 2605–2615.

(13) Lin, V. J.; Koenig, J. L. Raman Studies of Bovine Serum Albumin. *Biopolymers* **1976**, *15* (1), 203–218.

(14) Compiano, A.-M.; Romano, J.-C.; Garabetian, F.; Laborde, P.; de la Giraudièrea, I. Monosaccharide Composition of Particulate Hydrolysable Sugar Fraction in Surface Microlayers From Brackish and Marine Waters. *Mar. Chem.* **1993**, *42* (3–4), 237–251.

(15) Russell, L. M.; Hawkins, L. N.; Frossard, A. A.; Quinn, P. K.; Bates, T. S. Carbohydrate-like Composition of Submicron Atmospheric Particles and Their Production From Ocean Bubble Bursting. *Proc. Natl. Acad. Sci. U. S. A.* **2010**, *107* (15), 6652–6657.

(16) Hawkins, L. N.; Russell, L. M. Polysaccharides, Proteins, and Phytoplankton Fragments: Four Chemically Distinct Types of Marine Primary Organic Aerosol Classified by Single Particle Spectromicroscopy. *Adv. Meteorol.* **2010**, *2010*, 1–14.

(17) Gao, Q.; Leck, C.; Rauschenberg, C.; Matrai, P. A. On the Chemical Dynamics of Extracellular Polysaccharides in the High Arctic Surface Microlayer. *Ocean Sci.* **2012**, *8* (4), 401–418.

(18) van Pinxteren, M.; Müller, C.; Iinuma, Y.; Stolle, C.; Herrmann, H. Chemical Characterization of Dissolved Organic Compounds From Coastal Sea Surface Microlayers (Baltic Sea, Germany). *Environ. Sci. Technol.* **2012**, *46* (19), 10455–10462.

(19) Cunliffe, M.; Engel, A.; Frka, S.; Gašparović, B.; Guitart, C.; Murrell, J. C.; Salter, M.; Stolle, C.; Upstill-Goddard, R.; Wurl, O. Sea Surface Microlayers: A Unified Physicochemical and Biological Perspective of the Air–Ocean Interface. *Prog. Ocean.* **2013**, *109*, 104–116.

(20) Wang, A.; Freeman, J. J.; Jolliff, B. L.; Chou, I.-M. Sulfates on Mars: A Systematic Raman Spectroscopic Study of Hydration States of Magnesium Sulfates. *Geochim. Cosmochim. Acta* **2006**, *70* (24), 6118–6135.

(21) Zhang, Y.-H.; Chan, C. K. Study of Contact Ion Pairs of Supersaturated Magnesium Sulfate Solutions Using Raman Scattering of Levitated Single Droplets. *J. Phys. Chem. A* **2000**, *104* (40), 9191–9196.

(22) Shahzad, M. I.; Giorcelli, M.; Shahzad, N.; Guastella, S.; Castellino, M.; Jagdale, P.; Tagliaferro, A. Study of Carbon Nanotubes Based Polydimethylsiloxane Composite Films. *J. Phys. Conf. Ser.* **2013**, *439*, 12010.

(23) Gügi, B.; Le Costaouec, T.; Burel, C.; Lerouge, P.; Helbert, W.; Bardor, M. Diatom-Specific Oligosaccharide and Polysaccharide Structures Help to Unravel Biosynthetic Capabilities in Diatoms. *Mar. Drugs* **2015**, *13* (9), 5993–6018.

(24) Parkinson, J.; Gordon, R. Beyond Micromachining: The Potential of Diatoms. *Trends Biotechnol.* **1999**, *17* (5), 190–196.

(25) Marron, A. O.; Alston, M. J.; Heavens, D.; Akam, M.; Caccamo, M.; Holland, P. W. H.; Walker, G. A Family of Diatom-Like Silicon Transporters in the Siliceous Loricate Choanoflagellates. *P. Roy. Soc. B-Biol. Sci.* **2013**, *280* (1756), 20122543.

(26) Laucks, M. L.; Sengupta, A.; Junge, K.; Davis, E. J.; Swanson, B. D. Comparison of Psychro-Active Arctic Marine Bacteria and Common Mesophillic Bacteria Using Surface-Enhanced Raman Spectroscopy. *Appl. Spectrosc.* **2005**, *59* (10), 1222–1228.

(27) Kamnev, A. A.; Tarantilis, P. A.; Antonyuk, L. P.; Bespalova, L. A.; Polissiou, M. G.; Colina, M.; Gardiner, P. H. E.; Ignatov, V. V. Fourier Transform Raman Spectroscopic Characterisation of Cells of the Plant-Associated Soil Bacterium Azospirillum Brasilense Sp7. *J. Mol. Struct.* **2001**, *563–564*, 199–207.

(28) Wustman, B. A.; Lind, J.; Wetherbee, R.; Gretz, M. R. Extracellular Matrix Assembly in Diatoms III . Organization of Fucoglucuronogalactans within the Adhesive Stalks of Achnanthes Longipes. *Plant Physiol.* **1998**, *116*, 1431–1441.

(29) Vorum, H.; Brodersen, R.; Kragh-hansen, U.; Pedersen, A. O. Solubility of Long-Chain Fatty Acids in Phosphate Buffer at pH 7.4. *Biochim. Biophys. Acta* **1992**, *126*, 135–142.

(30) Babak, V. G.; Skotnikova, E. A.; Lukina, I. G.; Pelletier, S.; Hubert, P.; Dellacherie, E. Hydrophobically Associating Alginate Derivatives: Surface Tension Properties of Their Mixed Aqueous Solutions with Oppositely Charged Surfactants. *J. Colloid Interface Sci.* **2000**, *225* (2), 505–510.

(31) Verdugo, P.; Alldredge, A. L.; Azam, F.; Kirchman, D. L.; Passow, U.; Santschi, P. H. The Oceanic Gel Phase: A Bridge in the DOM–POM Continuum. *Mar. Chem.* **2004**, *92* (1–4), 67–85.

(32) Morris, H. S.; Estillore, A. D.; Laskina, O.; Grassian, V. H.; Tivanski, A. V. Quantifying the Hygroscopic Growth of Individual Submicrometer Particles with Atomic Force Microscopy. *Anal. Chem.* **2016**, *88* (7), 3647–3654.

(33) Petters, M. D.; Kreidenweis, S. M. A Single Parameter Representation of Hygroscopic Growth and Cloud Condensation Nucleus Activity-Part 3: Including Surfactant Partitioning. *Atmos. Chem. Phys.* **2007**, *7*, 1081–1091.

(34) Cochran, R. E.; Laskina, O.; Jayarathne, T.; Laskin, A.; Laskin, J.; Lin, P.; Sultana, C. M.; Lee, C.; Moore, K. A.; Cappa, C. D.; et al. Analysis of Organic Anionic Surfactants in Fine (PM2.5) and Coarse (PM10) Fractions of Freshly Emitted Sea Spray Aerosol. *Environ. Sci. Technol.* **2016**, *50*, 2477–2486.

(35) Panagiotopoulos, C.; Sempéré, R. Analytical Methods for the Determination of Sugars in Marine Samples: A Historical Perspective and Future Directions. *Limnol. Oceanogr. Methods* **2005**, *3*, 419–453.

(36) Jayarathne, T.; Stockwell, C. E.; Yokelson, R. J.; Nakao, S.; Stone, E. A. Emissions of Fine Particle Fluoride from Biomass Burning. *Environ. Sci. Technol.* **2014**, *48*, 12636–12644.

(37) Cai, D.; Neyer, A.; Kuckuk, R.; Heise, H. M. Raman, Mid-Infrared, Near-Infrared and Ultraviolet–Visible Spectroscopy of PDMS Silicone Rubber for Characterization of Polymer Optical Waveguide Materials. *J. Mol. Struct.* **2010**, *976* (1–3), 274–281.